Tracing the contribution of dust origins on deposition and

phytoplankton carbon uptake in global oceans

Yaxin Liu^a, Yunting Xiao^a, Lehui Cui^a, Qinghao Guo^a, Yiyang Sun^a, Pingqing Fu^a, Cong-qiang Liu^a, Jialei Zhu ^{a,*} ^a Institute of Surface-Earth System Science, School of Earth System Science, Tianjin University, Tianjin 300072, China * Corresponding author. Email address: zhujialei@tju.edu.cn

ABSTRACT

Dust provides iron, essential for marine phytoplankton growth, altering their carbon uptake capacity and affecting the global carbon cycle. However, due to the limited availability of observational parameters applied in evaluation models, there remains uncertainty in the contribution of marine dust deposition to carbon uptake. Here, we quantified the separate contributions of eleven major dust sources to dust deposition and marine ecological response to dust-borne iron in eight ocean regions based on a series of simulations constrained by multiple global observation datasets of iron solubility and total iron concentration in the oceans as well as iron content in the dust. Our simulations indicate that dust deposition could supply 11.1 Tg yr⁻¹ of total iron and 0.4 Tg yr⁻¹ of dissolved iron to the oceans. However, the study is limited by sparse observations and simplified assumptions, and further observations in undersampled regions would help to better constrain phytoplankton responses to dust-derived iron.

Keywords: Dust deposition; Carbon uptake; Fe supply; Source apportionment

1 Introduction

44

45

46

47

48

49

50

51

52

53

54

55

56

57

58

59

60

61

62

63

64

65

Dust aerosol, the main component of atmospheric aerosols from arid and semiarid areas, is the dominant exogenous input of Iron (Fe) to the surface of the ocean (Raiswell et al., 2012; Tagliabue et al., 2017). Dust carries various micronutrients that can be transported thousands of kilometers and deposited in remote ocean regions, ultimately resulting in the redistribution of nutrient elements (Jickells et al., 2005; Hamilton et al., 2022). Fe is an essential micronutrient for phytoplankton growth and can limit primary productivity in regions termed high nutrient, low chlorophyll (HNLC) regions, which comprise ~30% of the global ocean (Moore et al., 2013). Several sources of Fe in the ocean have been identified, primarily including atmospheric dust, coastal inputs, and hydrothermal fluids (Tagliabue et al., 2017; Tagliabue et al., 2015; Boyd et al., 2010). When Fe enters the upper ocean, dFe is absorbed by marine organisms, such as phytoplankton and bacteria. After the organisms die, Fe is returned to the sediment, or, through physical processes, may be resuspended and re-enter the water column, completing the cycle (Boyd et al., 2010). However, large amounts of fluvial and glacial particulate Fe are trapped in coastal areas (Poulton et al., 2002), and hydrothermal inputs are promptly precipitated at depth in the ocean (Lough et al., 2023). Therefore, dust is a major external source and dust deposition carrying Fe can promote photosynthesis and plankton growth, thereby impacting the carbon cycle and atmospheric carbon dioxide (CO₂) (Mahowald et al., 2011; Johnson et al., 2013; Kanakidou et al., 2018; Pavia et al., 2020; Westberry et al., 2023). Nevertheless, quantitative assessments of the linkage between dust sources and their effects on marine biogeochemical cycles in various oceanic regions are still lacking (Shoenfelt et al., 2019;
 Hamilton et al., 2023).

68

69

70

71

72

73

74

75

76

77

78

79

80

81

82

83

84

85

86

87

One key reason current studies struggle to estimate marine phytoplankton carbon uptake to dust-borne Fe is the uncertainties in assessing the dissolved Fe (dFe) (Hamilton et al., 2023). Changes in the supply of dFe within its range of uncertainty can lead to substantial differences in phytoplankton carbon uptake (Dietze et al., 2017; Watson et al., 2000; Spolaor et al., 2013), since only dFe can be utilized by phytoplankton instead of all Fe in deposited dust (Mahowald et al., 2005; Shaked et al., 2005). Thus, accurately evaluating the dFe supply from dust deposition over the ocean is vital to assessing the marine phytoplankton carbon uptake caused by dust. The Fe content in dust and solubility of dust-borne Fe vary among different dust source regions (Struve et al., 2022). Therefore, determining the contributions of dust source regions to various oceans separately is essential for accurately assessing the dust-borne dFe. Previous studies have predominantly focused on investigating the spatiotemporal variations of global or regional dust emissions (Choobari et al., 2014; Wang et al., 2014; Ginoux et al., 2001; Mahowald et al., 2003; Tegen et al., 2004), as well as the dust deposition fluxes to oceans (Zheng et al., 2016; Kok et al., 2021). Some studies evaluated global Fe cycle and Fe deposition using models (Myriokefalitakis et al., 2015; Zhang et al., 2015). However, the specific dust and Fe contributions of the various dust sources to the distinct oceans remain insufficiently understood, hindering a systematic understanding of the Fe supply relationships between sources and oceans, as well as their seasonal variations and underlying mechanisms. Moreover, dust usually

undergoes complex atmospheric chemical processes during long distance transport, resulting in enhanced solubility of Fe within the dust particles (Longo et al., 2016; Li et al., 2017; Félix-Bermúdez et al., 2020; Kurisu et al., 2024). Consequently, the dFe content in dust transported to remote oceanic regions is typically higher than that in dust from the sources (Shi et al., 2012). The content of total Fe in aerosols can vary by a factor of 2 (Mahowald et al., 2005; Mahowald et al., 2011). Due to the complexity and uncertainty of atmospheric chemical processes including acidic reactions and photoreduction, accurately simulating the dFe content in dust deposited in remote oceanic regions is challenging. In previous studies, the Fe content of deposited dust is usually assumed to be 3.5%, while its solubility is assumed to be 2% (Jickells et al., 2005; Hamilton et al., 2022; Mahowald et al., 2005; Mahowald et al., 2017), overlooking their variability in different sources and chemical processes during transport. This assumption may lead to uncertainties in evaluating the Fe deposition from dust sources and the input of Fe to the oceans.

The struggle to accurately quantify the relationship between Fe availability and marine phytoplankton carbon uptake is a key problem limiting the evaluation of the marine phytoplankton carbon uptake to dust-borne input of Fe. Previous studies have verified that dust-borne inputs of Fe can enhance the carbon uptake, thereby impacting the carbon cycle (Bishop et al., 2002; Patra et al., 2007; Ziegler et al., 2013; Kobayashi et al., 2021). The large decline in atmospheric CO₂ during past glacial periods coincided with an increase in observed Southern Ocean marine productivity and substantial dust deposition as recorded in marine sediments and ice cores (Ziegler et al., 2013; Lambert

et al., 2008; Wolff et al., 2010). Model simulations also indicate that the Fe fertilization from glaciogenic dust played an important role in enhancing carbon storage and declining atmospheric CO₂ concentration (Kobayashi et al., 2021). However, quantifying the marine phytoplankton carbon uptake caused by dust-borne inputs of Fe remains highly uncertain due to the complex processes during dust transport and the difficulty in quantifying phytoplankton growth induced by Fe supply from dust deposition. Several studies have tried to quantify the responses of marine biogeochemistry to dust deposition on large scales based on model simulations and observations (Mahowald et al., 2009; Mahowald et al., 2010; Ito et al., 2020), but the results vary largely due to the different global parameterization models. Given the complex and dynamic environmental conditions experienced by phytoplankton growth in the ocean, the ratios of carbon to nutrients in exported organic matter have long been used to simplify biogeochemical cycles (Twining et al., 2015; Wiseman et al., 2023). Ratios, such as Fe to carbon (Fe: C) in phytoplankton cells, help determine the efficiency of the biological export of carbon (Wiseman et al., 2023). In HNLC regions, Fe is the main limiting factor inducing phytoplankton blooms, and consequently influencing phytoplankton carbon uptake (Matrin et al., 1990; Boyd et al., 2007). In low nutrient, low chlorophyll (LNLC) regions, Fe can also alleviate nutrient-limiting pressure, and dust addition can stimulate nitrogen fixation, thereby promote phytoplankton growth and impact the carbon cycle (Zhang et al., 2019; Okin et al., 2011; Mills et al., 2004). Therefore, Fe is a significant limiting nutrient over global oceans, and Fe: C ratios in phytoplankton cells could be considered as a bridge to

110

111

112

113

114

115

116

117

118

119

120

121

122

123

124

125

126

127

128

129

130

estimate the global carbon uptake by phytoplankton to dust deposition. In this study, marine phytoplankton carbon uptake specifically refers to the amount of carbon uptake by phytoplankton as a result of dust-derived dFe input, estimated using the Fe: C ratio in phytoplankton cells under the assumption of Fe-limited marine conditions. Wiseman et al (2023) proposed a clearly dynamic relationship between phytoplankton Fe: C ratios and ambient dFe concentrations, making it possible to quantify the variations of marine phytoplankton carbon uptake caused by dust-borne inputs of dFe which could provides integrated insights into past climatic events and aids future marine-based CO₂ removal initiatives for climate mitigation.

In this study, we conducted a series of sensitivity experiments using the Community Earth System Model (CESM) to apportion the contributions of various dust sources to dust deposition and Fe supply in different marine areas globally. By incorporating the Fe content of dust from diverse source as well as observations of oceanic Fe solubility and content from numerous sites, we calculated the carbon uptake by phytoplankton resulting from dust deposition in various marine areas. This research employs an observation-driven approach, providing a new perspective for assessing the impact of dust on the global carbon cycle and attempting to establish a more accurate and detailed link between different dust sources and carbon uptake by phytoplankton in various marine areas.

2 Methods

2.1 Community Earth System Model

CESM version 1.2.2 (Hurrell et al., 2013) is employed in this study, which is a community tool to figure out the behavior of Earth's climate. In the model, atmospheric dust is emitted from the land by wind in the Community Land Model (CLM) (Mahowald et al., 2006) and then transported and processed in the atmosphere by the Community Atmosphere Model (CAM) (Neale et al., 2012). The wind friction speed, vegetation cover, and soil moisture are key factors which could determine the soil erodibility and dust emission. The dust emission scheme employed into CLM based on the Dust Entrainment and Deposition (DEAD) model of Zender et al (2003). More details could be found in Technical Description of CLM v4.0 (Oleson et al., 2010) and CAM5 Scientific Guide (Neale et al., 2012).

In dust model, the total vertical dust mass flux (F_j , kg m⁻² s⁻¹), from the ground into transport bin j is calculated by the following function:

$$F_j = TS f_m \alpha Q_S \sum_{i=1}^{I} M_{i,j} \tag{1}$$

Where T is a tuning factor that compensates for the DEAD model's sensitivity to horizontal and temporal resolution and equals 5×10^{-4} , S is the source erodibility factor set to 1 and serves as a place holder, f_m is a dimensionless fraction representing the exposed bare soil, α is the sandblasting mass efficiency (m⁻¹), Q_S is the total horizontally saltating mass flux (kg m⁻¹ s⁻¹), and $M_{i,j}$ is the dimensionless mass fraction of each source mode i carried in different bin j.

2.2 Regions classification and sensitivity experiments

171

172

173

174

175

176

177

178

179

180

181

182

183

184

185

186

187

188

189

190

191

192

To identify the contributions of dust source regions to the oceans, eleven main dust source regions and eight ocean regions were classified. Most dust is emitted from the so-called "dust belt", which includes northern Africa, the Middle East, central Asia, and the northwest of China and the Mongolian deserts. Small amounts of dust are emitted from Australia, southern Africa, and North and South America. In addition to considering the primary dust sources, the varying iron content of the dust is also a factor in defining the dust source regions. Ultimately, we divided dust sources over the world into eleven source regions that together account for the overwhelming total of desert dust emissions identified in models. Eleven dust source regions are Northwest Africa (NWAf), Northeast Africa (NEAf), Middle Africa (MAf), South Africa (SAf), North America (NAm), South America (SAm), West Asia (WAs), Middle-North Asia (MNAs), East Asia (EAs), South Asia (SAs), and Australia (AU), respectively. The apportionment of the source regions partially follows the definition provided by Kok et al (2021), with the main difference being that we divided Asia into more regions due to variations in iron content. 30°S and 30°N are the boundaries for dividing the difference ocean regions. The north of 30°N is North Pacific Ocean (NP), North Atlantic Ocean (NA), Mediterranean Sea (MS), respectively. The south of 30°S is Southern Ocean (SO). In addition, between the 30°N and 30°S is Equatorial Pacific Ocean (EP), Equatorial Atlantic Ocean (EA), Equatorial Indian Ocean (EI), respectively. In total, eleven dust source regions corresponding with eight deposit ocean regions are classified in this study as shown in

Fig. 1 and Table 1.

193

194

195

196

197

198

199

200

201

202

203

204

205

206

207

208

209

210

211

212

213

214

Three main HNLC regions as selected and defined by Aumont et al (2006) include the Southern Ocean (SO) south of 40°S, the equatorial Pacific (EP) between 5°S - 5°N and 180°W - 80°W, and the subarctic North Pacific (NP) north of 40°N and spanning 140°E - 120°W (Fig. 1 and Table 1).

We conducted five-year simulations with a spatial resolution of $1.9^{\circ} \times 2.5^{\circ}$, a 30min time step, and monthly output frequency to investigate the characteristics of global dust emission and deposition. Each simulation was preceded by a one-year spin-up and used a 30-minute model time step. A baseline simulation including global dust emissions was performed. In each experimental case, emissions from a specific dust source region were turned off, and the difference between this scenario and the baseline case was considered as the dust emission and deposition from that particular dust source region. The model configuration included 30 vertical layers. We employed prescribed aerosol emissions that repeat annually, based on emission inventories representative of the year 2000. The configuration imposes a climatological forcing by applying an identical annual emission cycle throughout the simulation period. Prescribed climatological sea ice and sea surface temperature from Hadley Centre were used to drive the (https://climatedataportal.metoffice.gov.uk/). climate Environmental boundary conditions were derived from the default CESM surface dataset for the year 2000, which includes land cover, soil properties, vegetation distribution, and dust source regions. Atmospheric initial conditions were specified using the standard initialization file provided for CAM.

2.3 Fe Solubility and dissolved Fe concentration data

215

216

217

218

219

220

221

222

223

224

225

226

227

228

229

230

231

232

233

234

235

236

To accurately estimating the Fe supply to the ocean from dust deposition, we used varying Fe content data for different dust source regions based on ten-year-averaged percentages of elements over desert regions provided in Zhang et al (2015). The Fe contents in NWAf, MAf, NEAf, SAf, NAm, SAm, WAs, MNAs, EAs, SAs and AU are 2.00, 2.65, 1.91, 2.47, 2.38, 2.28, 2.20, 1.76, 2.08, 2.17 and 2.70%, respectively. Fe solubility is also a key factor to estimate the carbon uptake of phytoplankton to dust deposition. Since the complex particle-aging processes during dust transport would influence the solubility of dust-born Fe (Longo et al., 2016), the observed Fe solubility in different oceans were used to constrain the Fe solubility in specific marine areas. The observation data, introduced in Ito et al (2019), included 774 sites of Fe solubility across various oceans. To mitigate the risk of overestimating the contribution of dust-borne Fe, Fe solubility data were filtered to retain only values below 6.0%, based on the studies by Shi et al (2011a), Shi et al (2009), Shi et al (2011b), Journet et al (2008), Tapp et al (2010) and Scanza et al (2018). Shi et al (2011) found that Fe solubility ranged from approximately 0.1% to 0.8% in various size fractions of Saharan soil samples. After cloud processing, Fe solubility of Saharan soil sample could increase to 3.5% (Shi et al., 2009). Shi et al (2011b) measured potential Fe solubility of Saharan soil dust samples approaching 6%. However, Fe solubility of dust could increase during transport, which is attributed to the complex atmospheric chemical processes, including acidic reactions and photoreduction (Longo et al., 2016; Li et al., 2017). Journet et al

(2008) and Trapp et al (2010) found maximum solubility values of 5.25% and 5.8%,

respectively, by measuring African dust collected over the Atlantic Ocean, Mediterranean Sea, and Barbados, which had experienced atmospheric transport. Consequently, we filtered the Fe solubility data to retain only values below 6.0%. Since the Fe solubility data used in this study are derived from multiple sources, not solely from dust, there is a possibility that the filtered-out Fe solubility data may be overestimated if regarded as representative of dust, as these data could originate from other sources, such as combustion. Scanza et al (2018) showed that the global Fe solubility from both dust and combustion sources, as simulated, ranged from 0% to 20%. Ultimately, 514 data points were retained and interpolated to a resolution of 1.9° ×2.5° for this study. The mean Fe solubility interpolated from observations is 2.8%, which is comparable to the assumed value of dust Fe solubility (2%) by previous studies (Jickells et al., 2005), but incorporates spatial distribution (Fig. S1). The dFe concentration data is a necessary factor for calculating the Fe: C ratio in phytoplankton cells. The dFe concentration data used in this study is from the **GEOTRACES** Intermediate Data Product 2021 Version 2 (https://www.bodc.ac.uk/geotraces/data/idp2021/). GEOTRACES is an international study of the marine biogeochemical cycles of trace elements and isotopes, and provides a broad coverage of observational data on aerosol nutrients (Schlitzer et al., 2018). A total of 15970 data of dFe concentration across 3304 sites over ocean were obtained. Data overlapping on the same sites were averaged, and the resulting observed dFe concentration over ocean were interpolated into a resolution of 1.9°×2.5° for this study

237

238

239

240

241

242

243

244

245

246

247

248

249

250

251

252

253

254

255

256

257

258

(Fig. S2).

2.4 Inverse distance weighting interpolation

We employed the inverse distance weighting (IDW) method, a widely used spatial interpolation technique, to interpolate observation data on Fe solubility and dFe concentration to a resolution of 1.9°×2.5°. The globe was divided into a grid matrix of 144×96 cells based on simulation results from CESM. Observations were matched to the grid matrix using spatial coordinates and subsequently interpolated using the IDW method. Spatial distances between each interpolation grid and observation locations were calculated iteratively. Weight functions were then applied to these distances to compute a weighted average, yielding the interpolated results.

The function to calculate the weight is as follows:

$$w_i = \frac{1}{d_i^P} \tag{2}$$

Here, w_i represents the weight of the *i*-th observation, d_i is the distance between the observation location and the interpolation point, and P is a tuning factor set to 3 for this interpolation.

The weights are applied to calculate a weighted average, yielding the interpolated results. The formula for calculating the weighted average is expressed as follows:

$$z(x,y) = \frac{\sum_{i=1}^{N} w_i z_i}{\sum_{i=1}^{N} w_i}$$
 (3)

Here, z(x, y) is the interpolated result, N is the number of the observations, (x, y) denotes the coordinates of the i-th observation, w_i is its weight, and z_i is the observed data.

To prevent data from a single site from affecting oceanic regions on both sides of a landmass, we delineated land-sea boundaries during interpolation. However, the uneven global distribution and limited number of observations and complex land-sea boundaries could lead to interpolation uncertainty. Refining interpolation methods may reduce the uncertainty and improve estimates the impact of Fe on phytoplankton carbon uptake.

2.5 Calculation of marine phytoplankton carbon uptake

The contribution of each dust source region to the dissolved Fe deposition in various marine areas can be calculated based on dust deposition rates and Fe solubility.

Then, Fe: C ratios in phytoplankton cells are employed to calculate marine phytoplankton carbon uptake caused by dust deposition with the function as follows:

$$C = \frac{D * Fe_{con} * Fe_{sol}}{gQfe} \tag{4}$$

where C is the amount of marine phytoplankton carbon uptake driven by dust deposition, D (Tg) is the amount of dust from source regions and deposit to oceans, Fe_{con} (%) is the Fe content for different dust source region, and Fe_{sol} (%) is the solubility of Fe over various oceans.

Fe: C ratio in phytoplankton cells (gQfe) is defined to be a linear function of the dFe concentration in seawater (Sunda et al, 1995), which is a vital link for estimating the marine phytoplankton carbon uptake to variations of dust-borne inputs of Fe. The following is the function to calculate Fe: C ratio in phytoplankton cells used in this study (Wiseman et al., 2023):

$$gQfe = \min(gQfe_max, \max(gQfe_min, gQfe_max \times \frac{dFe}{FeOpt}))$$
 (5)

where gQfe is the Fe: C ratio in phytoplankton cells, gQfe_max is the prescribed maximum Fe: C, gQfe min is the prescribed minimum Fe: C, dFe is the local

concentration of dissolved Fe (nmol/L), and FeOpt refers to the Fe concentration at which Fe: C ratio in phytoplankton cells reaches its maximum value. In this study, we used a broad Fe: C ratio range in phytoplankton cells (3-90 µmol Fe mol⁻¹ C) and an FeOpt of 1.75 nM for all phytoplankton groups, as proposed by Wiseman et al (2023), to estimate phytoplankton carbon uptake driven by Fe from dust. Given that Fe is the primary limiting nutrient in HNLC regions, we also calculated phytoplankton carbon uptake attributable to dust deposition in these regions. However, using the Fe: C ratio in phytoplankton cells to estimate the response of phytoplankton carbon uptake to dust deposition may introduce some uncertainty, because this method does not fully account for potential co-limiting factors such as light availability and the interactive effects of multiple micronutrients. The results, especially in non-HNLC regions, is only a hypothetical research results, and the uncertainty needs to be further reduced after being enriched with experimental and observational data.

3 Results

- 3.1 Spatial and temporal characteristics of global dust emission and deposition over the oceans
- Our simulations indicate a global annual average dust emission of 2071.5 Tg (Fig.
- 316 2). The highest dust emission concentrated in North Africa (i.e. NEAf and NWAf),
- 317 surrounding the Sahara Desert. Dust emission from NEAf and NWAf accounts for 58.0%
- of global dust emission, with NEAf exhibiting a stronger intensity of dust emission
- compared to NWAf. Dust emitted from WAs (317.7 Tg yr⁻¹) is also a key contributor to
- global dust emission, accounting for 15.3% of global dust emission. The northeastern

region of the Arabian Desert, located on the Arabian Peninsula, is the primary area of dust emission within WAs, while the east of the Caspian Sea is also notable for its strong dust emissions, attributed to the presence of the Kyzylkum Desert and Karakum Desert (Fig. 2). Furthermore, the SAs and EAs regions are also high emission sources, including the Taklamakan Desert, Gobi Desert, and several small deserts such as the Badain Jaran Desert, Tengger Desert, Ulan Buh Desert, and Kubuchi Desert. Dust emissions from SAf, America (NAm, SAm), and MNAs are minor contributors to global dust emissions, each accounting for ~1% of the total dust emission. The contributions of the main dust sources to global dust emissions in this study are comparable with the results presented by Jickells et al (2005) and Wang et al (2024). Global dust emissions exhibit large seasonal variations, with emissions during spring and summer (663.0 and 667.1 Tg season⁻¹) being approximately 70-90% higher than those in autumn and winter (349.3 and 392.2 Tg season⁻¹) (Fig. S3). This is largely attributed to the pronounced seasonal variations in dust emissions from the Asian region (Fig. S3 and 3). Dust emissions in EAs and SAs during spring (67.2 and 94.7 Tg) are 813.6% and 436.2% higher than those in winter (7.4 and 17.7 Tg) in EAs and SAs, respectively. During winter, surface temperatures in SAs and EAs can drop to below -30°C, leading to soil freezing and reduced dust emissions (Fig. S4). The seasonal variations of dust emission in the Southern Hemisphere, such as SAf, SAm and AU, are similar. In these areas, dust emissions peak in autumn with SAf, SAm, and AU emitting 10.0, 3.6 and 26.6 Tg, respectively. In comparison, spring is the season with low dust

321

322

323

324

325

326

327

328

329

330

331

332

333

334

335

336

337

338

339

340

341

342

emission season in these regions (3.21, 1.38 and 11.2 Tg) (Fig.3).

There are 560.2 Tg dust deposited into ocean every year (Fig. 4), representing 27.0% of the annual global dust emission. Wet deposition dominates the dust deposition, accounting for 77.4% of the total dust deposition to the ocean. As shown in Fig. 4, the dust deposition over EA (235.0 Tg yr⁻¹) and EI (132.9 Tg yr⁻¹) is highest among oceans around the world. Dust depositions in the EP, NP, MS, RS and SO regions show a decreasing trend, with annual dust deposition of 53.8, 46.0, 28.2, 26.2 and 19.1 and 18.9 Tg, respectively. NA has the lowest dust deposition of 18.9 Tg yr⁻¹, indicating that northwestward transport is not the primary direction for dust from Africa. In addition, the contributions of dry deposition to dust deposition in all oceans are generally less than 30%, much lower than that of wet deposition, except in the RS and MS. The proportions of dry deposition in RS and MS are 52.0% and 46.4%, respectively, due to their relatively small areas with low precipitation and proximity to dust sources.

Global marine dust deposition in summer (209.4 Tg season⁻¹) is higher than other seasons (Fig. S5) (147.5 Tg season⁻¹ in spring, 96.8 Tg season⁻¹ in autumn and 106.5 Tg season⁻¹ in winter). In summer, dust deposition in EI increases sharply, rising by 337.6% compared to spring, primarily due to the increase of wet deposition (Fig. S6 and S7). The large reduction in dust deposition in EA during autumn, which is ~60 Tg lower than in other seasons, is the primary reason for the lowest global dust deposition during this period. As EA is a key source of marine dust deposition, this sharp decline in autumn emissions is a major contributor to the global decrease in dust deposition. (Fig. 3). Generally, high dust deposition occurs in spring and summer, while low dust deposition occurs in autumn and winter in all oceans except for SO and MS. (Fig. 3).

Dust deposition in SO peaks in autumn, while it is lowest in the spring (Fig. 3). The MS experiences its lowest dust deposition in summer, with 3.3 Tg, a pattern that contrasts with the higher summer deposition seen in other oceanic regions. Moreover, seasonal variations of dust deposition are drastic in RS, EI and NP with changes of 626.1%, 600.4% and 550.0%, respectively.

3.2 Annual and seasonal contributions of dust sources to deposition over ocean

The source apportionment of dust deposition over eight oceans were conducted through a series of sensitivity experiments. Dust from NWAf and NEAf are the major contributors to dust deposition over EA, NA, MS and EP, accounting for more than 50% of dust deposition in each of these oceans (Fig. 5). Dust from NEAf is also the dominant contributor to dust deposition over RS, while dust from NWAf makes only a minor contribution due to a small portion of dust from NWAf being transported eastward (Fig. 5). EA is the ocean with the highest dust deposition over the world, which is primarily attributed to the dust transported westward from NWAf and NEAf. Dust from NWAf (46.0%) contributes slightly more to deposition over EA than dust from NEAf (44.2%), as a greater amount of dust from NWAf can be westward transported to EA than from NEAf (Fig. 5).

EI is the ocean with the second highest dust deposition, primarily due to the overwhelming southward transport of dust from WAs, accounting for 59.1% (Fig. 5). The second largest contributor to dust deposition over EI is dust from NEAf, accounting for 22.7%, mainly owing to the primary eastward transport from NEAf. The following contributor to EI's dust deposition is dust from SAs, accounting for 10.0% (Fig. 5).

Dust deposition in other oceans is comparatively lower than that in the EA and EI regions, but each with distinct source characteristics. EP and NP have similar dust deposition, accounting for 9.6% and 8.2% of total dust deposition over global oceans, respectively, but their major contributors are quite different. The major contributors to dust deposition over EP are NWAf and NEAf, while they are EAs and SAs for NP (Fig. 5). Moreover, dust deposition over NP is mainly from Asia except for MNAs, while dust from MNAs is primarily deposited over EP (Fig. 5). Dust deposition over MS and RS is similar (29.5 and 26.2 Tg yr⁻¹), accounting for 5.3% and 4.7% of total dust deposition over the ocean, respectively. Dust from NEAf and NWAf dominate the dust deposition over MS, accounting for 98.6%. However, NEAf is the primary contributor to dust deposition over RS, while dust from NWAf contributes little (Fig. 5). Additionally, dust deposition over SO is mainly from dust sources in the Southern Hemisphere (i.e. AU, SAf, and SAm).

As mentioned above, the largest global marine dust deposition occurs in summer dominated by the large dust deposition over EI in summer (Fig. S5). The seasonal variations in contributions from dust sources to oceans further explain this increase in summer. The primary contributor to dust deposition over EI is dust from WAs, which primarily transports southward and deposits over EI through the year (Fig. S8). In summer, dust emission from WAs peaks with the highest ratio of deposition to emission in WAs, which is 20% higher (up to 47.4%) than in other seasons (Fig. 3 and S3). The proportion of dust from WAs deposited over EI in summer (85.3%) is 10-30% higher than in other seasons (Fig. S8). In addition, dust from NEAf is predominantly

transported eastward in summer, leading to an increase of \sim 30% compared to other seasons in the amount of dust from NEAf deposited over EI (Fig. S8). Dust emission from NEAf is also highest in summer, with the ratio of deposition to emission slightly higher by \sim 7% than in other seasons. Therefore, dust deposition over EI in summer is six times higher than in other seasons.

The dust deposition over EA in autumn is 29.4% lower than that in other seasons (Fig. 3). Dust from NWAf and NEAf are consistent major sources of dust deposition over EA, contributing ~90% of the dust deposition to EA through the year (Fig. S8). Dust emissions from NWAf and NEAf are 59.1% and 45.7% lower in autumn compared to their peak seasons (spring for NWAf and summer for NEAf) (Fig. 3). Therefore, the decrease in dust deposition over EA in autumn is primarily due to reduced dust emissions from these two key contributors.

The lowest amount of dust deposition over oceans typically occurs in autumn and winter, except for MS, where it occurs in summer (Fig. 3). Dust from NWAf and NEAf are consistently accounts for more than 98% of total dust deposition over MS as major contributors (Fig. S8). However, in summer, less dust from NWAf and NEAf is transported and deposited over MS, decreasing by ~10% and ~6%, respectively, compared to other seasons.

Dust deposition over RS, EI, NP and EP exhibits the largest seasonal variations among ocean areas, with variations of 626.3%, 600.4%, 550.0% and 424.9%, respectively. NEAf and WAs have consistently been the primary sources of dust deposition in the RS region, contributing over 90% of the total, though their respective

contributions show noticeable seasonal variations (Fig. S8). During the summer, the eastward transport of dust from NEAf increases, leading to a 15-21% rise in its contribution to dust deposition in the RS region compared to other seasons (Fig. S8). The contribution of dust from NEAf shows a significant increase only in summer, further widening the gap with seasons of lower dust deposition. This is a key factor in the 626.3% increase in dust deposition over the RS in summer compared to winter (Fig. 3). The seasonal variation in dust deposition over the NP region is driven by the large seasonal variations in Asian dust emissions as its primary source (Fig. S8). Dust from EAs and SAs consistently contributing over 80% of the dust deposition over the NP area with emission peak in spring (Fig. S8). As a result, dust deposition over NP is much higher in spring than in other seasons, with an increase of 550.0% compared to winter. The primary sources of dust deposition over EP are also dust sources in Asian, except during summer (Fig. S8). The primary contributors to dust deposition over EP in summer are NWAf and NEAf, accounting for 73.0% (41.6% for NWAf and 31.4% for NEAf). Dust from NWAf and NEAf leads to 2 to 26 times more dust deposition over the EP during the summer compared to other seasons, resulting in a large seasonal disparity in dust deposition. Therefore, dust deposition over EP in summer is 424.9% higher than that in winter. 3.3 Spatiotemporal patterns in phytoplankton carbon uptake driven by dust-borne iron supply According to the function (4), the Fe: C ratio in phytoplankton cells is a crucial

431

432

433

434

435

436

437

438

439

440

441

442

443

444

445

446

447

448

449

450

451

452

453

factor in calculating phytoplankton carbon uptake induced by dust deposition into the

observations (Ito et al., 2019; GEOTRACES Intermediate Data Product Group, 2023) to the same grid as our simulations. An Fe: C ratio in phytoplankton cells lower than the optimal value indicates large marine phytoplankton carbon uptake driven by the same amount of Fe supply. Increased Fe supply usually can enhance carbon uptake by phytoplankton, but only soluble Fe is bioavailable and Fe: C ratio is lower than optimal value, making the solubility of Fe key to the phytoplankton's carbon uptake to dust deposition. The interpolated result of Fe solubility showed that high Fe solubility primarily occurred in EA and NA, particularly in north-central EA. Relatively high Fe solubility was also found in the regions spanning 105°W-130°W and 45°E-75°E in the SO (Fig. S1). We estimated global phytoplankton carbon uptake induced by dust deposition using the Fe: C ratio in phytoplankton cells. Because Fe is the primary limiting nutrient in HNLC regions, we additionally provided a separate estimate for these regions.

Our simulations indicate that annual dust deposition supplies 11.1 Tg of Fe to the global ocean, of which 0.4 Tg is dFe, driving a carbon uptake of 5.6 Pg C yr⁻¹ by phytoplankton. High dust-borne dFe primarily occurs in EI (1.1 × 10⁻¹ Tg yr⁻¹), EA (1.7 × 10⁻¹ Tg yr⁻¹), and MS (1.7 × 10⁻² Tg yr⁻¹) (Fig. S9). The high Fe: C ratio in phytoplankton cells is primarily occurred in EA, particularly in the north-central of EA (Fig. S10). The mean Fe: C ratio in phytoplankton cells in EA is the highest, which is 62.5 μmol Fe mol⁻¹ C. The NP and EP near America, as well as NA, exhibit relatively high Fe: C ratios in phytoplankton cells (Fig. S10). The average Fe: C ratios in phytoplankton cells in NP, EP, and NA are 19.6, 27.6, and 28.0 μmol Fe mol⁻¹ C,

respectively. Large marine phytoplankton carbon uptake driven by dust deposition occurs primarily in EA, EI and RS (Fig. 6), which exhibit positive ecological responses to dust deposition, with uptake values of 2.2, 1.8 and 0.5 Pg C yr⁻¹, respectively. The following areas are NP (0.3 Pg C vr⁻¹), EP (0.3 Pg C vr⁻¹), NA (0.2 Pg C vr⁻¹) and MS (0.2 Pg C yr⁻¹). The marine phytoplankton carbon uptake driven by dust deposition is minimal in the SO (0.1 Pg C yr⁻¹), accounting for only ~3% of the total marine phytoplankton carbon uptake driven by global dust deposition. The spatial distribution of marine phytoplankton carbon uptake driven by dust deposition closely mirrors that of dust deposition. In EA, marine phytoplankton carbon uptake driven by dust deposition decreases from east to west, while in EI, the northwestward region exhibits high values (Fig. 6). Despite the large Fe: C ratio in phytoplankton cells in EA, which means the carbon uptake by phytoplankton is not sensitive to dust-born Fe supply, it remains the region with the largest marine phytoplankton carbon uptake to dust deposition, accounting for 41.3% of the marine phytoplankton carbon uptake induced by dust deposition (Fig. 6 and S10). This strong response is supported by the highest Fe supply from dust deposition (4.7 Tg yr⁻¹) and Fe solubility (6.7% in average) in EA. The intensity of marine phytoplankton carbon uptake driven by dust deposition in RS is much higher than that in other oceans, mainly because of the lowest Fe: C ratio in phytoplankton cells in RS (7.0 μmol Fe mol⁻¹ C) (Fig. 6 and S10). In addition, compared to the role in global dust deposition over the oceans, the contributions of marine phytoplankton carbon uptake driven by dust deposition in EP is smaller due to low Fe solubility (1.9%) and high Fe: C (27.6 µmol Fe mol⁻¹ C).

476

477

478

479

480

481

482

483

484

485

486

487

488

489

490

491

492

493

494

495

496

The global phytoplankton marine carbon uptake driven by dust deposition in summer is 2.1 Pg C season⁻¹ while that is ~1.0 Pg C in other seasons (1.4 Pg C season⁻¹ ¹ in spring, 0.9 Pg C season⁻¹ in autumn and 1.2 Pg C season⁻¹ in winter) (Fig. S11). During summer, phytoplankton in EI, EA and RS contribute most to the global marine carbon uptake induced by dust deposition, with EI at 0.9 Pg C, EA at 0.5 Pg C and RS at 0.3 Pg C, in addition, the marine phytoplankton carbon uptake over EI and RS are much higher in summer than in other seasons (Fig. 7). Except for summer, EA has the largest marine phytoplankton carbon uptake driven by dust deposition among all ocean areas (Fig. 7). Generally, high marine phytoplankton carbon uptake usually occurred in spring and summer, and low marine phytoplankton carbon uptake occurred in autumn and winter, in addition to SO, MS and EA (Fig. 7). The seasonal variations of marine phytoplankton carbon uptake in SO and MS are dominated by the seasonal variation in dust deposition. Nevertheless, the seasonal changes in marine phytoplankton carbon uptake in EA differ from the seasonal pattern of its dust deposition. High marine phytoplankton carbon uptake in EA occurs in winter (0.7 Pg C) and spring (0.7 Pg C), while low marine phytoplankton carbon uptake occurs in autumn (0.4 Pg C) and summer (0.5 Pg C) (Fig. 7). In comparison, high dust deposition in EA occurs in spring (65.67 Tg), winter (61.8 Tg) and summer (61.2 Tg), the lowest dust deposition occurs in autumn (46.4 Tg) (Fig. 3). These differences are mainly due to the difference in the seasonal pattern between Fe: C ratio in phytoplankton cells and dust deposition in EA. The seasonal variations and spatial distribution of carbon uptake for new growth in the EA region are largely influenced by the Fe: C ratio in phytoplankton cells, in addition

498

499

500

501

502

503

504

505

506

507

508

509

510

511

512

513

514

515

516

517

518

to the impact of dust deposition. High marine phytoplankton carbon uptake in EA during winter and spring is mainly distributed in the middle region, where Fe: C ratios in phytoplankton cells are relatively low (Fig. S10). In contrast, during autumn and summer, high marine phytoplankton carbon uptake is centered in the northern EA, where Fe: C ratios in phytoplankton cells are high (Fig. S10).

520

521

522

523

524

525

526

527

528

529

530

531

532

533

534

535

536

537

538

539

540

541

Recognizing Fe as the primary limiting nutrient in HNLC regions, we provided a separate estimate for these regions. The results show that annual dust deposition provides 0.8 Tg Fe to HNLC regions, of which 2.2×10⁻² Tg is dFe, causing a marine phytoplankton carbon uptake of 0.2 Pg C yr⁻¹. The marine phytoplankton carbon uptake driven by dust deposition occurred in the HNLC region over NP, SO and EP is 1.6×10⁻¹ 1 , 7.2×10^{-2} and 9.3×10^{-3} Pg C yr⁻¹, respectively. The estimation of global marine phytoplankton carbon uptake attributed to dust deposition is 5.6 Pg C yr⁻¹, which may be overestimated due to the assumption that every grid where dust deposition occurs over the ocean responds to its Fe supply. Therefore, the actual annual marine phytoplankton carbon uptake due to dust deposition worldwide is likely between 0.2 Pg C yr⁻¹ and 5.6 Pg C yr⁻¹. In addition, phytoplankton carbon uptake driven by dust deposition in HNLC regions is the highest in spring (9.6×10⁻² Pg C season⁻¹), compared with summer (6.5×10⁻² Pg C season⁻¹), autumn (6.3×10⁻² Pg C season⁻¹), and winter (2.1×10⁻² Pg C season⁻¹). Dust-driven phytoplankton carbon uptake is the highest in HNLC regions of the NP across all seasons, except in winter, accounting for 86.1% in spring. In winter, phytoplankton in the SO contribute the most to dust-driven marine carbon uptake in HNLC regions, with 1.1×10⁻² Pg C (~50.2%), while the NP accounts for ~45.6%.

3.4 Source apportionments of marine phytoplankton carbon uptake induced by dust deposition

Dust from NEAf (1.7 Pg C yr⁻¹), NWAf (1.5 Pg C yr⁻¹), and WAs (1.3 Pg C yr⁻¹) are the primary drivers of marine phytoplankton carbon uptake induced by dust deposition (Fig. 7). NEAf, NWAf and WAs make their largest contributions to marine phytoplankton carbon uptake during the summer, contributing 0.7, 0.4 and 0.7 Pg C yr⁻¹, respectively (Fig. 7). They (NEAf, NWAf and WAs) all contribute least in autumn with contributions of 0.2, 0.2, and 0.1 Pg C yr⁻¹, respectively (Fig. 7). Examining the seasonal variation in contributions from dust sources to global dust-driven carbon uptake of marine phytoplankton, contribution from EAs exhibits the largest seasonal variation. In spring, marine phytoplankton carbon uptake induced by dust from EAs is about ten times higher than in winter (Fig. 7). Dust from MAf and MNAs also shows a 5-6 fold difference in their contributions to global marine phytoplankton carbon uptake across different seasons, but their overall contributions remain only ~2% (Fig. 7 and 8).

The heterogeneity in Fe solubility and Fe: C ratios in phytoplankton cells across

global oceans leads to difference in the contributions of dust sources to marine dust deposition and phytoplankton carbon uptake. The greatest contributors to marine phytoplankton carbon uptake in EP differ from those that contribute most to dust deposition in the region (Fig. 5 and 8). The dust from AU is the dominant contributor to marine phytoplankton carbon uptake driven by dust deposition over EP, accounting for 30.4%, while the dust from NWAf and NEAf, the major contributors to dust deposition over EP, only accounts for 17.2% and 15.6%, respectively (Fig. 5 and 8).

Dust from AU is the third largest supplier of Fe to dust deposition over EP, following NWAf and NEAf. This is primarily because dust deposition over EP from NWAf and NEAf is mainly concentrated in the northeast, near the southwest coast of NAm, where Fe: C ratios in phytoplankton cells are relatively higher compared to the areas dust from AU is deposited over EP (Fig. S10). The contribution (33.4%) of dust from AU to marine phytoplankton carbon uptake in SO is lower compared to its contribution (51.5%) to dust deposition over SO (compare Fig. 5 and 8), mainly due to high Fe: C ratio in phytoplankton cells in the southeast of AU, which is the primary area of dust from AU deposit over SO (Fig. S10). On the contrary, the contributions of the dust from SAf to carbon uptake for new growth in SO is larger compared to its contributions to dust deposition owing to low Fe: C ratio in phytoplankton cells in the southeast of SAf, where is the main regions of SAf's dust deposit over SO (Fig. S10). Therefore, spatial variations in Fe solubility and the Fe: C ratio in phytoplankton cells will to some extent lead to differences between the spatial distribution characteristics of dust deposition and the resulting spatial distribution characteristics of marine phytoplankton carbon uptake. Globally, dust from NEAf is the largest contributor to the marine phytoplankton carbon uptake driven by dust deposition which accounts for 30.0% (1.7 Pg C yr⁻¹) (Fig. 8), followed by NWAf (1.5 Pg C yr⁻¹), accounting for 26.2%. WAs (1.3 Pg C yr⁻¹) and SAs (0.4 Pg C yr⁻¹) are also important sources to annual total marine carbon uptake induced by dust deposition, accounting for 24.0% and 6.4%. Dust from AU and EAs account for 4.3% and 3.4% of the global marine carbon uptake for new growth driven by dust deposition, dust from SAf and MAf account for 3.4% and 3.2%, respectively.

565

566

567

568

569

570

571

572

573

574

575

576

577

578

579

580

581

582

583

584

585

Dust from SAm, MNAs and NAm contribute relatively lower to the marine carbon uptake driven by dust deposition, less than 1%, respectively.

587

588

589

590

591

592

593

594

595

596

597

598

599

600

601

602

603

604

605

606

607

608

The seasonal variation in marine phytoplankton carbon uptake is most pronounced in RS (Fig. 7). The highest marine phytoplankton carbon uptake in RS occurred in summer at 0.3 Pg C, which is about ten times higher than in winter, resulting in a drastic seasonal fluctuation occurred in RS (Fig. 7). During summer, dust deposition over RS increases from almost all dust sources, particularly NEAf and WAs (Fig. S12). Specifically, dust from NEAf contributes 0.2 Pg C, and dust from WAs contributes 0.1 Pg C to marine phytoplankton carbon uptake driven by dust deposition in RS. Additionally, the lowest Fe: C ratio in phytoplankton cells in RS further enhances the marine carbon uptake for new growth driven by dust deposition during summer. During winter, dust deposition in RS primarily from NEAf and WAs, could leading to 1.2×10⁻¹ ² Pg C and 2.1×10⁻² Pg C of marine phytoplankton carbon uptake (Fig. S12). The carbon uptake for new growth induced by dust deposition over NP and EI also exhibits large seasonal variations, with differences between seasons reaching 542.1% and 438.8%, respectively (Fig. 7). The highest marine phytoplankton carbon uptake driven by dust deposition in NP occurred in spring at 0.2 Pg C, while the lowest occurred in winter at 2.9×10⁻² Pg C. The marine phytoplankton carbon uptake in NP throughout the year is predominantly attributed to the dust from Asia, particularly from EAs and SAs (Fig. S12). The pronounced seasonal variations in dust emissions from EAs and SAs are the primary reasons for the large seasonal changes in carbon uptake induced by dust deposition in the NP (Fig. 3). During summer, marine phytoplankton carbon uptake driven by dust deposition in EI peaks at 0.9 Pg C, contrasting with its lowest uptake in autumn at 0.2 Pg C (Fig. 7). This fluctuation is primarily driven by changes in dust deposition over EI (Fig. 3). Substantial dust from NEAf and WAs deposits in EI during summer, sharply diminishing in autumn (Fig. S8).

4 Discussion and conclusions

609

610

611

612

613

614

615

616

617

618

619

620

621

622

623

624

625

626

627

628

629

Identifying the contribution of dust sources to deposition over oceans is key to quantify the dust-borne input of dFe to the ocean, which is critical for understanding its impact on marine ecosystems, the carbon cycle, and climate. In this study, CESM was employed to identify the contributions of various dust source regions to dust deposition, revealing that EA and EI are the major contributors to global dust deposition over the ocean, with contributions of 41.6% and 23.7%, respectively. These contributions are primarily due to the westward transport of dust from NEAf and NWAf, the largest dust emission sources, to the EA region, and the dominant southward transport of dust from WAs to EI. Additionally, dust deposition over the RS exhibits the largest seasonal variations among ocean areas, with fluctuations of 626.3%, primarily due to a sudden large increase in deposited dust from NEAf over RS occurring exclusively in summer. Based on the contribution relationship, we quantified the total Fe and dFe supplied to the ocean due to dust deposition and used the Fe: C ratio in phytoplankton cells to identify its effect on carbon uptake by phytoplankton in various oceans, we found that dust deposition onto the ocean supplies 11.1 Tg yr⁻¹ of Fe and 0.4 Tg yr⁻¹ of dFe, leading to a marine phytoplankton carbon uptake of 5.6 Pg C yr⁻¹. Large marine phytoplankton carbon uptake driven by dust deposition occurs primarily in EA and EI, leading to 2.3 and 1.7 Pg C yr⁻¹, respectively, because large amount of dust deposition over EA and EI. Marine phytoplankton carbon uptake driven by dust deposition is highest in summer (2.1 Pg C season⁻¹), followed by spring (1.4 Pg C season⁻¹) and winter (1.2 Pg C season⁻¹) 1), with the lowest uptake occurred in autumn (0.9 Pg C season⁻¹). Marine phytoplankton carbon uptake caused by dust deposition in summer over the RS is 843.0% higher than in other seasons, representing the largest seasonal variation among ocean areas. This significant variation is primarily due to the sharp increase in dust deposition from NEAf during summer and the lowest Fe: C ratio in phytoplankton cells in RS. Compared with previous studies, Myriokefalitakis et al (2018) reported that total Fe emissions from dust sources in various models (CAM4, IMPACT, GEOS-Chem, and TM4-ECPL) ranged from 38 to 134 Tg total Fe yr⁻¹, with a mean value of 71.5 \pm 43 Tg total Fe yr⁻¹, which is comparable with our result of 42.5 Tg Fe yr⁻¹. Their simulations of soluble Fe from mineral dust ranged from 0.3 to 1.0 Tg dFe yr⁻¹, with a mean value of approximately 0.7 ± 0.3 Tg dFe yr⁻¹. The amount of Fe supplied to the ocean from dust deposition in our study (11.1 Tg yr⁻¹) is close to the lower end of other global estimates (12.94 ± 0.31 Tg yr⁻¹) presented by Myriokefalitakis et al (2022).

630

631

632

633

634

635

636

637

638

639

640

641

642

643

644

645

646

647

648

649

650

651

The amount of dust deposition is fundamental in determining the marine carbon uptake for new growth to Fe supply from dust. Consequently, the relationship between dust deposition in various oceans and their respective dust sources elucidates the link between carbon uptake for new growth in each marine region and its dust sources. Currently, few studies have quantified the large-scale response of the carbon cycle to

dust deposition. Mahowald et al (2010) demonstrated that dust deposition trends increase ocean productivity by 6% over the 20th century, leading to marine carbon uptake of 8 Pg C (equivalent to 4ppm in atmospheric CO₂). They combined the ecosystem component of the Biogeochemical Elemental Cycling (BEC) ocean model and a carbonate chemistry module to calculate pCO2 and air-sea CO2 flux to estimate the variation of carbon. Although their carbon uptake estimate differs in magnitude and approach from ours, it offers a valuable point of reference. The air-sea CO₂ flux reflects the net oceanic uptake of atmospheric CO₂, which is determined by the ultimate fate of fixed carbon (e.g., export, remineralization, or trophic transfer). In contrast, the Fe: C ratio in phytoplankton cells reflects their physiological response to iron enrichment, directly influencing their capacity for photosynthetic carbon fixation. As a portion of the fixed carbon is later released through respiration, remineralization, or physical mixing, estimates based on Fe: C ratios in phytoplankton cells generally exceed the amount of carbon that is ultimately sequestered and captured in net air-sea CO₂ fluxes. Although our carbon uptake estimates, based on Fe: C ratios in phytoplankton, may not be directly comparable to the air-sea CO₂ flux estimates presented by Mahowald et al. (2010), the two approaches represent different yet complementary stages of the oceanic carbon cycle. Our study focuses on the initial carbon fixation response triggered by dust-borne iron inputs, while Mahowald et al. (2010) evaluated the net carbon sequestration resulting from ocean-atmosphere CO₂ exchange. Additionally, their estimate of the influence on marine biogeochemistry was based on the increase of anthropogenic inorganic nitrogen and soluble Fe from atmospheric processing of dust

652

653

654

655

656

657

658

659

660

661

662

663

664

665

666

667

668

669

670

671

672

and combustion sources, rather than from dust alone. Westberry et al (2023) estimated that 2.55×10⁻² Pg C yr⁻¹ of primary production was supported by dust deposition onto the ocean. The primary reason for the discrepancies between their results and us depends on the differing methodologies employed. Westberry et al. (2023) employed an observation-based empirical approach, utilizing the Carbon-based Production Model (CbPM) to estimate the net primary production response to dust deposition by comparing ocean color properties during 4-day periods before and after dust events. In contrast, our study aimed to quantify phytoplankton carbon uptake by identifying the contributions of dFe from various dust source regions to the ocean and applying Fe: C ratios in phytoplankton cells. Additionally, the approach used by Westberry et al. (2023) primarily captures short-term biological responses through changes in chlorophyll and phytoplankton carbon biomass, but it does not account for delayed ecosystem feedbacks. As a result, CbPM-based analyses may underestimate longer-term or region-specific productivity enhancements driven by dFe, particularly in HNLC regions where phytoplankton growth is strongly Fe-limited. In such regions, the biological response to atmospheric Fe deposition may be delayed or only weakly evident in short-term changes in ocean color properties. Consequently, empirical models such as CbPM, which rely on brief pre- and post-event comparisons of satellite-derived chlorophyll and phytoplankton carbon, may difficult to fully capture the longer-term or more subtle productivity enhancements induced by dust-borne Fe inputs. Moreover, satellite data are susceptible to atmospheric conditions and cloud cover, and satellite-derived ocean color products often rely on empirical inversion models, which may also contribute to

674

675

676

677

678

679

680

681

682

683

684

685

686

687

688

689

690

691

692

693

694

the underestimation of their results. Furthermore, they provided limited insights into the evaluation of dust-induced marine phytoplankton carbon uptake, lacking a detailed analysis of the spatiotemporal variations and sources of this carbon up on a global scale. Our evaluation of marine phytoplankton carbon uptake was based on simulated dust deposition combined with multiple observation datasets, including global distribution of marine Fe solubility, total Fe concentration in the oceans, which would provide diverse perspectives and comprehensive view of marine ecological response to dust emission over the world.

The uncertainty of annual marine phytoplankton carbon uptake due to dust deposition (5.6 ± 0.2 Pg C yr⁻¹) was estimated by interannual variations. The primary uncertainty is the interannual variability in the magnitude of marine dust deposition (approximately 550-600 Tg yr⁻¹) and its spatial distribution. We also utilized dFe concentration data from the Coupled Model Intercomparison Project Phase 6 (CMIP6) to estimate marine phytoplankton carbon uptake driven by dust deposition. Based on dFe concentration data from CESM2 (2000-2014) historical simulations, the estimated marine phytoplankton carbon uptake driven by dust deposition was 2.2 Pg C yr⁻¹, while that from Geophysical Fluid Dynamics Laboratory Earth System Model version 4 (GFDL-ESM4) (2010-2014) was 3.2 Pg C yr⁻¹ (Fig. S13). It is important to note that Equation (4) is based on dissolved iron (dFe) concentrations. Some studies, such as Hamilton et al. (2020) and Bergas-Massó et al. (2023), report data for soluble Fe, which differs substantially from dFe. Specifically, colloidal Fe and complexing capacity—ranging from >200 kDa to <0.2 μm—are inferred from the difference

between the dissolved and soluble fractions (Boye et al., 2010). Compared to the estimates derived from observational data, the spatial distributions of marine phytoplankton carbon uptake from CMIP6 models (CESM2 and GFDL-ESM4) show similar global patterns, with high uptake mainly observed in the EA and EI, particularly in the northwestern EI. The use of CESM2 and GFDL-ESM4 dFe data resulted in approximately 61% and 43% reductions, respectively, in estimated marine phytoplankton carbon uptake relative to observation-based estimates. For CESM2based results, the reduction was particularly pronounced in the southern RS, where uptake decreased from 0.4 to 0.1 Pg C yr⁻¹; the western Arabian Sea (in the EI), from 1.8 to 0.5 Pg C yr⁻¹; and the north-central EA, from 2.2 to 0.7 Pg C yr⁻¹ (compare Fig. 6 and Fig. S13). For GFDL-ESM4-based results, notable reductions were also observed in the north-central EA (from 2.2 to 0.9 Pg C yr⁻¹) and the western Arabian Sea (from 1.8 to 0.7 Pg C yr⁻¹), whereas an evident increase occurred in the EP, from 0.3 to 0.7 Pg C yr⁻¹ (compare Fig. 6 and Fig. S13). Additionally, the uncertainties of the observed dFe data were assessed by comparing the observations with model data from CESM2 and GFDL-ESM4, extracted at the specific grid cells corresponding to the geographic locations of the observations. The results indicate that simulated values are often substantially lower than the observed data. Approximately 7% of the CESM2-simulated dissolved Fe data are at least ten times lower than the observed values, and about 1% are more than one hundred times lower. Similarly, about 4% of the GFDL-ESM4simulated dFe data are at least ten times lower than the observed values. On average, the dissolved Fe concentrations simulated by CESM2 and GFDL-ESM4 are \sim 4-5 times

718

719

720

721

722

723

724

725

726

727

728

729

730

731

732

733

734

735

736

737

738

lower than the observed values. The discrepancies between observed and simulated dFe can reach up to two orders of magnitude. As an inverse distance weighted interpolation method is used to estimate both Fe solubility and dFe concentrations, the spatial distribution and density of observational sites exert a significant influence on the interpolation results. For Fe solubility, observational data are dense in the EA, which may result in low interpolation uncertainty. In contrast, the central and southern EI are characterized by sparse observations, potentially leading to high interpolation uncertainty. For dFe, observational data are dense in both the EA and NA, supporting relatively accurate interpolation in these regions. In contrast, data scarcity in the southern EI may contribute to increased uncertainty. However, in the EA, where interpolation uncertainty is relatively low due to dense observational coverage, the modeled dFe concentrations significantly underestimate the dust-driven carbon uptake by marine phytoplankton compared to estimates based on observations. Specifically, the estimates based on CESM2 and GFDL-ESM4 are approximately 68% and 59% lower, respectively, than those derived from observed dFe data. These findings further underscore the importance of incorporating observational data in the estimation of the contribution of iron deposition to marine phytoplankton carbon uptake. Despite data scarcity and interpolation uncertainties, observation-based constraints substantially correct the underestimation of totally simulations, demonstrably lowering uncertainties in data-rich areas—with critical implications for optimizing future observing systems and observation-based methodologies. Compared with the results obtained using spatially variable parameters, the estimate of marine phytoplankton carbon uptake

740

741

742

743

744

745

746

747

748

749

750

751

752

753

754

755

756

757

758

759

760

based on constant values for Fe content in dust (3.5%), Fe solubility (2%), and a mean Fe: C ratio of 19.4 μmol Fe mol⁻¹ C in phytoplankton cells is approximately 21% lower. Using constant values also reduces the spatial variability of the results, leading to a distribution pattern that largely reflects the spatial intensity of dust deposition (Fig. S14). Compared the result with that obtained using unfiltered Fe solubility data, the marine carbon uptake for new growth attributed to dust deposition decreased by 54.1%, as the largest range of Fe solubility shifted from 50.0% to 6.0%. Although uncertainty remains in estimating the marine phytoplankton carbon uptake for new growth attributed to dust deposition, it can still provide a meaningful reflection of potential requirements of phytoplankton, it does provide an observation-based quantification for the specific contributions of dust depositions to marine phytoplankton carbon uptakes. We incorporated monthly dFe concentration data from CESM2 (2000-2014) and GFDL-ESM4 (2010-2014) historical simulations provided by CMIP6 to complement the sparse observational data, thereby attempting to better capture seasonal variations in marine phytoplankton carbon uptake. The monthly dFe data from CESM2 indicate that the total amount of global marine phytoplankton carbon uptake driven by dust deposition is 0.7 Pg C in summer, followed by 0.6 Pg C in spring, and 0.4 Pg C in both autumn and winter. The monthly dFe data from GFDL-ESM4 show that marine phytoplankton carbon uptake driven by dust deposition is 1.0 Pg C in both spring and summer, and 0.6 Pg C in both autumn and winter. Although the carbon uptake by marine phytoplankton due to dust deposition assessed using CESM2 and GFDL-ESM4 dFe data differed in value across four seasons, the spatial distribution remained relatively

762

763

764

765

766

767

768

769

770

771

772

773

774

775

776

777

778

779

780

781

782

consistent. (compare Fig. S15 and Fig. S16).

784

785

786

787

788

789

790

791

792

793

794

795

796

797

798

799

800

801

802

803

804

805

In this study, we used data from 514 sites of Fe solubility and 3340 sites of dFe concentration across various oceans to interpolate and calculate the Fe: C ratio in phytoplankton cells. However, the somewhat nonuniform distribution of marine observations across the vast spatial span of the study increases uncertainties in the interpolation of Fe solubility and dFe concentrations. Compared to dFe concentration, there is substantially less data available on the distribution of Fe solubility. More measurements and consistent measurement techniques would aid in the assessment of Fe solubility in the future. We adopt a parameterization scheme from previous studies, assuming a linear relationship between cellular Fe: C ratios and dFe concentrations and using a piecewise linear formula to describe this dependency. However, using this approach to assess global marine phytoplankton carbon uptake in response to Fe supplied by dust deposition has certain limitations. The linear relationship reported in the original experiments was derived from a limited number of phytoplankton species under controlled conditions, and it is uncertain whether it applies universally to all phytoplankton groups across diverse oceanic regions, given the physiological and ecological differences among species. Moreover, the approach we used does not explicitly account for luxury uptake of Fe, in which cells may continue to accumulate intracellular Fe beyond what is required for immediate growth. Ignoring this process introduces uncertainty in the assessment of phytoplankton carbon uptake, particularly during transient high-iron events such as dust deposition, riverine input, or upwelling. We assumed that phytoplankton in both HNLC and LNLC regions might respond to

dust deposition as a maximum estimate, considering Fe is particularly important for nitrogen fixing phytoplankton in LNLC regions. However, the phytoplankton growth by dust addition in LNLC regions relies not only on Fe, but also on phosphorus. Therefore, future estimations in LNLC regions should account for other nutrients to achieve more accurate results. The approach used to estimate Fe: C ratios in phytoplankton cells considers not only dust-borne Fe, but also other aerosol sources, such as pyrogenic and anthropogenic emissions, which often contain Fe with high solubility. As a result, applying such ratios to estimate marine phytoplankton carbon uptake driven solely by dust-derived Fe may lead to some degree of overestimation, particularly in remote ocean regions where dust is the predominant or only Fe source. We assumed that every grid where dust deposition occurred over the ocean all responded to its Fe supply to estimate its impact on marine phytoplankton carbon uptake, but this response also depends on phytoplankton distribution and species, potentially leading to an overestimation of the marine ecological response to carbon uptake. Phytoplankton growth is not unlimited with an increase in Fe, which heightens the risk of overestimating the marine ecological response to carbon uptake in high dust regions. Therefore, a reasonable growth threshold should be considered based on further observations and experiments.

824

825

806

807

808

809

810

811

812

813

814

815

816

817

818

819

820

821

822

823

Data availability

826 GEOTRACES intermediate data is available at 827 https://www.bodc.ac.uk/geotraces/data/idp2021/.

Code availability

828

831

834

835

836

837

838

839

840

842

The codes used to produce these results are available from the corresponding author upon reasonable request.

Acknowledgments

This study was supported by the National Key R&D Plan (Grant No. 2022YFE0135000).

Author contributions

Y.L. and J.Z. conceptualized the framework of study. Y.L. constructed the dataset and carried out the statistical analysis under the guidance of J.Z. Y.X. provided the codes of interpolation, C.L., Q.G. and Y.S. interpreted the results and improved figures presentation. P.F. and C.L. reviewed the manuscript and experiment. All authors contributed to the writing of the paper.

Competing Interests

The authors declare that they have no conflict of interest.

References

- 844 Aumont, O. and Bopp, L.: Globalizing results from ocean in situ iron fertilizat
- ion studies, Glob. Biogeochem. Cycles, 20, 10.1029/2005GB002591, 2006.
- 846 Bergas-Massó, E., Ageitos, M. G., Myriokefalitakis, S., Miller, R. L., van Noij
- e, T., Le Sager, P., Pinto, G. M., and García-Pando, C. P.: Pre-Industrial,
- Present and Future Atmospheric Soluble Iron Deposition and the Role of
- Aerosol Acidity and Oxalate Under CMIP6 Emissions, Earths Future, 11,
- e2022EF00335310. 1029/2022EF003353, 2023.
- 851 Bishop, J. K. B., Davis, R. E., and Sherman, J. T.: Robotic observations of du
- st storm enhancement of carbon biomass in the North Pacific, Science, 29
- 853 8, 817-821, 10.1126/science.1074961, 2002.
- Boyd, P. W. and Ellwood, M. J.: The biogeochemical cycle of iron in the oce
- an, Nat. Geosci., 3, 675-682, 10.1038/ngeo964, 2010.
- Boyd, P. W., Jickells, T., Law, C. S., Blain, S., Boyle, E. A., Buesseler, K. O.,
- Coale, K. H., Cullen, J. J., de Baar, H. J. W., Follows, M., Harvey, M.,
- Lancelot, C., Levasseur, M., Owens, N. P. J., Pollard, R., Rivkin, R. B., S
- armiento, J., Schoemann, V., Smetacek, V., Takeda, S., Tsuda, A., Turner,
- S., and Watson, A. J.: Mesoscale iron enrichment experiments 1993-2005:
- Synthesis and future directions, Science, 315, 612-617, 10.1126/science.113
- 862 1669, 2007.
- Boye, M., Nishioka, J., Croot, P., Laan, P., Timmermans, K. R., Strass, V. H.,
- Takeda, S., and de Baar, H. J. W.: Significant portion of dissolved organic

- Fe complexes in fact is Fe colloids, Mar Chem, 122, 20-27, 10.1016/j.ma
- rchem.2010.09.001, 2010.
- 867 Choobari, O. A., Zawar-Reza, P., and Sturman, A.: The global distribution of
- mineral dust and its impacts on the climate system: A review, Atmos. Re
- s., 138, 152-165, 10.1016/j.atmosres.2013.11.007, 2014.
- 870 Dietze, H., Getzlaff, J., and Loeptien, U.: Simulating natural carbon sequestrati
- on in the Southern Ocean: on uncertainties associated with eddy parameter
- izations and iron deposition, Biogeosciences, 14, 1561-1576, 10.5194/bg-14-
- 873 1561-2017, 2017.
- Félix-Bermúdez, A., Delgadillo-Hinojosa, F., Torres-Delgado, E. V., and Munoz-
- Barbosa, A.: Does Sea Surface Temperature Affect Solubility of Iron in M
- ineral Dust? The Gulf of California as a Case Study, J. Geophys. Res. Oc
- eans., 125, 10.1029/2019JC015999, 2020.
- 878 Gao, Y., Kaufman, Y. J., Tanré, D., Kolber, D., and Falkowski, P. G.: Seasona
- l distributions of aeolian iron fluxes to the global ocean, Geophys. Res. L
- ett., 28, 29-32, 10.1029/2000GL011926, 2001.
- 881 GEOTRACES Intermediate Data Product Group. The GEOTRACES intermediat
- e data product 2021v2 (IDP2021v2). NERC EDS British Oceanographic D
- ata Centre NOC. 10.5285/ff46f034-f47c-05f9-e053-6c86abc0dc7e (2023).
- 684 Ginoux, P., Chin, M., Tegen, I., Prospero, J. M., Holben, B., Dubovik, O., and
- Lin, S. J.: Sources and distributions of dust aerosols simulated with the
- 886 GOCART model, J. Geophys. Res. Atmos., 106, 20255-20273, 10.1029/200

- 887 0JD000053, 2001.
- Hamilton, D. S., Baker, A. R., Iwamoto, Y., Gasso, S., Bergas-Masso, E., Deut
- ch, S., Dinasquet, J., Kondo, Y., Llort, J., Myriokefalitakis, S., Perron, M.
- 890 M. G., Wegmann, A., and Yoon, J.-E.: An aerosol odyssey: Navigating nu
- trient flux changes to marine ecosystems, Elementa-Sci Anthrop., 11, 10.15
- 892 25/elementa.2023.00037, 2023.
- 893 Hamilton, D. S., Perron, M. M. G., Bond, T. C., Bowie, A. R., Buchholz, R.
- R., Guieu, C., Ito, A., Maenhaut, W., Myriokefalitakis, S., Olgun, N., Rath
- od, S. D., Schepanski, K., Tagliabue, A., Wagner, R., and Mahowald, N.
- 896 M.: Earth, Wind, Fire, and Pollution: Aerosol Nutrient Sources and Impact
- s on Ocean Biogeochemistry, Annu. Rev. Mar. Sci., 14, 303-330, 10.1146/
- 898 annurev-marine-031921-013612, 2022.
- Hamilton, D. S., Moore, J. K., Arneth, A., Bond, T. C., Carslaw, K. S., Hants
- on, S., Ito, A., Kaplan, J. O., Lindsay, K., Nieradzik, L., Rathod, S. D., S
- 901 canza, R. A., and Mahowald, N. M.: Impact of Changes to the Atmospher
- 902 ic Soluble Iron Deposition Flux on Ocean Biogeochemical Cycles in the
- Anthropocene, Global Biogeochemical Cycles, 34, e2019GB006448. 10.102
- 904 9/2019GB006448, 2020.
- 905 Hurrell, J. W., Holland, M. M., Gent, P. R., Ghan, S., Kay, J. E., Kushner, P.
- J., Lamarque, J. F., Large, W. G., Lawrence, D., Lindsay, K., Lipscomb,
- W. H., Long, M. C., Mahowald, N., Marsh, D. R., Neale, R. B., Rasch,
- 908 P., Vavrus, S., Vertenstein, M., Bader, D., Collins, W. D., Hack, J. J., Kie

- 909 hl, J., and Marshall, S.: The Community Earth System Model A Framewor
- 910 k for Collaborative Research, Bull. Am. Meteorol. Soc., 94, 1339-1360, 1
- 911 0.1175/BAMS-D-12-00121.1, 2013.
- 912 Ito, A., Ye, Y., Yamamoto, A., Watanabe, M., and Aita, M. N.: Responses of
- ocean biogeochemistry to atmospheric supply of lithogenic and pyrogenic i
- 914 ron-containing aerosols, Geol. Mag., 157, 741-756, 10.1017/S001675681900
- 915 1080, 2020.
- 916 Ito, A., Myriokefalitakis, S., Kanakidou, M., Mahowald, N. M., Scanza, R. A.,
- 917 Hamilton, D. S., Baker, A. R., Jickells, T., Sarin, M., Bikkina, S., Gao, Y.,
- Shelley, R. U., Buck, C. S., Landing, W. M., Bowie, A. R., Perron, M.
- 919 M. G., Guieu, C., Meskhidze, N., Johnson, M. S., Feng, Y., Kok, J. F., N
- enes, A., and Duce, R. A.: Pyrogenic iron: The missing link to high iron
- 921 solubility in aerosols, Sci. Adv., 5, 10.1126/sciadv.aau7671, 2019.
- 922 Jickells, T. D., An, Z. S., Andersen, K. K., Baker, A. R., Bergametti, G., Broo
- 923 ks, N., Cao, J. J., Boyd, P. W., Duce, R. A., Hunter, K. A., Kawahata,
- H., Kubilay, N., laRoche, J., Liss, P. S., Mahowald, N., Prospero, J. M.,
- 925 Ridgwell, A. J., Tegen, I., and Torres, R.: Global iron connections betwee
- n desert dust, ocean biogeochemistry, and climate, Science, 308, 67-71, 10.
- 927 1126/science.1105959, 2005.
- 928 Johnson, M. S. and Meskhidze, N.: Atmospheric dissolved iron deposition to th
- e global oceans: effects of oxalate-promoted Fe dissolution, photochemical
- 930 redox cycling, and dust mineralogy, Geosci. Model Dev., 6, 1137-1155, 10.

- 931 5194/gmd-6-1137-2013, 2013.
- 932 Journet, E., Desboeufs, K. V., Caquineau, S., and Colin, J.-L.: Mineralogy as a
- 933 critical factor of dust iron solubility, Geophys. Res. Lett. 35, 10.1029/200
- 934 7GL031589, 2008.
- 935 Kanakidou, M., Myriokefalitakis, S., and Tsigaridis, K.: Aerosols in atmospheri
- c chemistry and biogeochemical cycles of nutrients, Environ. Res. Lett. 13,
- 937 10.1088/1748-9326/aabcdb, 2018.
- 938 Kobayashi, H., Oka, A., Yamamoto, A., and Abe-Ouchi, A.: Glacial carbon cy
- ole changes by Southern Ocean processes with sedimentary amplification,
- 940 Sci. Adv., 7, 10.1126/sciadv.abg7723, 2021.
- 941 Kok, J. F., Adebiyi, A. A., Albani, S., Balkanski, Y., Checa-Garcia, R., Chin,
- 942 M., Colarco, P. R., Hamilton, D. S., Huang, Y., Ito, A., Klose, M., Leung,
- D. M., Li, L., Mahowald, N. M., Miller, R. L., Obiso, V., Perez Garcia-
- Pando, C., Rocha-Lima, A., Wan, J. S., and Whicker, C. A.: Improved rep
- resentation of the global dust cycle using observational constraints on dust
- properties and abundance, Atmos. Chem. Phys., 21, 8127-8167, 10.5194/ac
- 947 p-21-8127-2021, 2021.
- 948 Kurisu, M., Sakata, K., Nishioka, J., Obata, H., Conway, T. M., Hunt, H. R.,
- 949 Sieber, M., Suzuki, K., Kashiwabara, T., Kubo, S., Takada, M., and Takah
- ashi, Y.: Source and fate of atmospheric iron supplied to the subarctic No
- 951 rth Pacific traced by stable iron isotope ratios, Geochim. Cosmochim. Act
- 952 a., 378, 168-185, 10.1016/j.gca.2024.06.009, 2024.

- Lambert, F., Delmonte, B., Petit, J. R., Bigler, M., Kaufmann, P. R., Hutterli,
- 954 M. A., Stocker, T. F., Ruth, U., Steffensen, J. P., and Maggi, V.: Dust-cli
- mate couplings over the past 800,000 years from the EPICA Dome C ice
- 956 core, Nature, 452, 616-619, 10.1038/nature06763, 2008.
- 957 Li, W., Xu, L., Liu, X., Zhang, J., Lin, Y., Yao, X., Gao, H., Zhang, D., Che
- 958 n, J., Wang, W., Harrison, R. M., Zhang, X., Shao, L., Fu, P., Nenes, A.,
- and Shi, Z.: Air pollution-aerosol interactions produce more bioavailable ir
- on for ocean ecosystems, Sci. Adv., 3, 10.1126/sciadv.1601749, 2017.
- 961 Longo, A. F., Feng, Y., Lai, B., Landing, W. M., Shelley, R. U., Nenes, A.,
- 962 Mihalopoulos, N., Violaki, K., and Ingall, E. D.: Influence of Atmospheric
- Processes on the Solubility and Composition of Iron in Saharan Dust, En
- 964 viron. Sci. Technol., 50, 6912-6920, 10.1021/acs.est.6b02605, 2016.
- 965 Lough, A. J. M., Tagliabue, A., Demasy, C., Resing, J. A., Mellett, T., Wyatt,
- N. J., and Lohan, M. C.: Tracing differences in iron supply to the Mid-At
- lantic Ridge valley between hydrothermal vent sites: implications for the a
- ddition of iron to the deep ocean, Biogeosciences, 20, 405-420, https://doi.
- 969 org/10.5194/bg-20-405-2023, 2023.
- 970 Luo, C., Mahowald, N., Bond, T., Chuang, P. Y., Artaxo, P., Siefert, R., Chen,
- 971 Y., and Schauer, J.: Combustion iron distribution and deposition, Global
- 972 Biogeochem. Cycles, 22, 10.1029/2007GB002964, 2008.
- 973 Mahowald, N.: Aerosol Indirect Effect on Biogeochemical Cycles and Climate,
- 974 Science, 334, 794-796, 10.1126/science.1207374, 2011.

- 975 Mahowald, N. M., Muhs, D. R., Levis, S., Rasch, P. J., Yoshioka, M., Zender,
- 976 C. S., and Luo, C.: Change in atmospheric mineral aerosols in response to
- 977 climate: Last glacial period, preindustrial, modern, and doubled carbon di
- 978 oxide climates, J. Geophys. Res. Atmos., 111, 10.1029/2005JD006653, 200
- 979 6.
- 980 Mahowald, N. M., Scanza, R., Brahney, J., Goodale, C. L., Hess, P. G., Moor
- 981 e, J. K., and Neff, J.: Aerosol Deposition Impacts on Land and Ocean Ca
- 982 rbon Cycles, Curr. Clim. Change Rep., 3, 16-31, 10.1007/s40641-017-0056-
- 983 z, 2017.
- Mahowald, N. M., Baker, A. R., Bergametti, G., Brooks, N., Duce, R. A., Jick
- 985 ells, T. D., Kubilay, N., Prospero, J. M., and Tegen, I.: Atmospheric globa
- 986 I dust cycle and iron inputs to the ocean, Global Biogeochem. Cycles, 19,
- 987 10.1029/2004GB002402, 2005.
- 988 Mahowald, N. M., Engelstaedter, S., Luo, C., Sealy, A., Artaxo, P., Benitez-Nel
- son, C., Bonnet, S., Chen, Y., Chuang, P. Y., Cohen, D. D., Dulac, F., He
- 990 rut, B., Johansen, A. M., Kubilay, N., Losno, R., Maenhaut, W., Paytan,
- 991 A., Prospero, J. A., Shank, L. M., and Siefert, R. L.: Atmospheric Iron D
- eposition: Global Distribution, Variability, and Human Perturbations, Annu.
- 993 Rev. Mar. Sci., 1, 245-278, 10.1146/annurev.marine.010908.163727, 2009.
- Mahowald, N. M., Kloster, S., Engelstaedter, S., Moore, J. K., Mukhopadhyay,
- 995 S., McConnell, J. R., Albani, S., Doney, S. C., Bhattacharya, A., Curran,
- 996 M. A. J., Flanner, M. G., Hoffman, F. M., Lawrence, D. M., Lindsay, K.,

- Mayewski, P. A., Neff, J., Rothenberg, D., Thomas, E., Thornton, P. E., a
- 998 nd Zender, C. S.: Observed 20th century desert dust variability: impact on
- climate and biogeochemistry, Atmos. Chem. Phys., 10, 10875-10893, 10.51
- 1000 94/acp-10-10875-2010, 2010.
- 1001 Mahowald, N. M. & Luo, C. A less dusty future? Geophys. Res. Lett. 30, 190
- 1002 3, 10.1029/2003GL017880, 2003.
- 1003 Matrin, J. H. Glacial-interglacial CO₂ change: the iron hypothesis. Paleoceanogr
- aphy, 5, 1-13, 10.1029/PA005i001p00001, 1990.
- 1005 Mills, M. M., Ridame, C., Davey, M., La Roche, J., and Geider, R. J.: Iron a
- nd phosphorus co-limit nitrogen fixation in the eastern tropical North Atla
- ntic, Nature, 429, 292-294, 10.1038/nature02550, 2004.
- 1008 Moore, C. M., Mills, M. M., Arrigo, K. R., Berman-Frank, I., Bopp, L., Boyd,
- 1009 P. W., Galbraith, E. D., Geider, R. J., Guieu, C., Jaccard, S. L., Jickells,
- T. D., La Roche, J., Lenton, T. M., Mahowald, N. M., Maranon, E., Mar
- inov, I., Moore, J. K., Nakatsuka, T., Oschlies, A., Saito, M. A., Thingsta
- d, T. F., Tsuda, A., and Ulloa, O.: Processes and patterns of oceanic nutri
- ent limitation, Nat. Geosci., 6, 701-710, 10.1038/NGEO1765, 2013.
- 1014 Myriokefalitakis, S., Daskalakis, N., Mihalopoulos, N., Baker, A. R., Nenes, A.,
- and Kanakidou, M.: Changes in dissolved iron deposition to the oceans d
- riven by human activity: a 3-D global modelling study, Biogeosciences, 12,
- 1017 3973-3992, 10.5194/bg-12-3973-2015, 2015.
- 1018 Myriokefalitakis, S., Bergas-Masso, E., Goncalves-Ageitos, M., Garcia-Pando, C.

- P., van Noije, T., Le Sager, P., Ito, A., Athanasopoulou, E., Nenes, A., K
- anakidou, M., Krol, M. C., and Gerasopoulos, E.: Multiphase processes in
- the EC-Earth model and their relevance to the atmospheric oxalate, sulfate,
- and iron cycles, Geosci. Model Dev., 15, 3079-3120, 10.5194/gmd-15-307
- 1023 9-2022, 2022.
- 1024 Myriokefalitakis, S., Ito, A., Kanakidou, M., Nenes, A., Krol, M. C., Mahowal
- d, N. M., Scanza, R. A., Hamilton, D. S., Johnson, M. S., Meskhidze, N.,
- Kok, J. F., Guieu, C., Baker, A. R., Jickells, T. D., Sarin, M. M., Bikkin
- a, S., Shelley, R., Bowie, A., Perron, M. M. G., and Duce, R. A.: Revie
- ws and syntheses: the GESAMP atmospheric iron deposition model interco
- mparison study, Biogeoscience, 15, 6659-6684, 10.5194/bg-15-6659-2018, 2
- 1030 018.
- Neale, R. B., Gettelman, A., Park, S., Chen, C.-C., Lauritzen, P. H., Williamso
- n, D. L., Conley, A. J., Kinnison, D., Marsh, D., Smith, A. K., Vitt, F.
- M., Garcia, R., Lamarque, J.-F., Mills, M. J., Tilmes, S., Morrison, H., Ca
- meron-Smith, P., Collins, W. D., Iacono, M. J., Easter, R. C., Liu, X., Gh
- an, S. J., Rasch, P. J., and Taylor, M. A.: Description of the NCAR Com
- munity Atmosphere Model (CAM 5.0), UCAR/NCAR Library, https://n2t.
- 1037 <u>net/ark:/85065/d7s46whd</u>, 2012.
- Okin, G. S., Baker, A. R., Tegen, I., Mahowald, N. M., Dentener, F. J., Duce,
- 1039 R. A., Galloway, J. N., Hunter, K., Kanakidou, M., Kubilay, N., Prospero,
- J. M., Sarin, M., Surapipith, V., Uematsu, M., and Zhu, T.: Impacts of at

- mospheric nutrient deposition on marine productivity: Roles of nitrogen, ph
- osphorus, and iron, Glob. Biogeochem. Cycles, 25, 10.1029/2010GB003858,
- 1043 2011.
- 1044 Oleson, W., Lawrence, M., Bonan, B., Flanner, G., Kluzek, E., Lawrence, J., L
- evis, S., Swenson, C., Thornton, E., Dai, A., Decker, M., Dickinson, R., F
- eddema, J., Heald, L., Hoffman, F., Lamarque, J., Mahowald, N., Niu, G.,
- Qian, T. T., Randerson, J., Running, S., Sakaguchi, K., Slater, A., Stöckli,
- 1048 R., Wang, A. H., Yang, Z. L., Zeng, X., Zeng, X.. Technical Description
- of version 4.0 of the Community Land Model (CLM) (No. NCAR/TN-478
- +STR). University Corporation for Atmospheric Research, 10.5065/D6FB50
- 1051 WZ, 2010.
- Patra, P. K., Moore, J. K., Mahowald, N., Uematsu, M., Doney, S. C., and Na
- kazawa, T.: Exploring the sensitivity of interannual basin-scale air-sea CO₂
- fluxes to variability in atmospheric dust deposition using ocean carbon cyc
- le models and atmospheric CO₂ inversions, J. Geophys. Res. Biogeoscience
- 1056 s, 112, 10.1029/2006JG000236, 2007.
- Pavia, F. J., Anderson, R. F., Winckler, G., and Fleisher, M. Q.: Atmospheric
- Dust Inputs, Iron Cycling, and Biogeochemical Connections in the South P
- acific Ocean from Thorium Isotopes, Glob. Biogeochem. Cycles, 34, 10.10
- 1060 29/2020GB006562, 2020.
- 1061 Poulton, S. W. and Raiswell, R.: The low-temperature geochemical cycle of iro
- n: From continental fluxes to marine sediment deposition, Am. J. Sci., 30

- 1063 2, 774-805, 10.2475/ajs.302.9.774, 2002.
- Raiswell, R. and Canfield, D. E.: The iron biogeochemical cycle past and pres
- ent, Geochem. Perspect., 1, 1-220, 10.7185/geochempersp.1.1, 2012.
- 1066 Scanza, R. A., Hamilton, D. S., Perez Garcia-Pando, C., Buck, C., Baker, A.,
- and Mahowald, N. M.: Atmospheric processing of iron in mineral and co
- mbustion aerosols: development of an intermediate-complexity mechanism s
- uitable for Earth system models, Atmos. Chem. Phys., 18, 14175-14196, 1
- 1070 0.5194/acp-18-14175-2018, 2018.
- 1071 Schlitzer, R., Anderson, R. F., Dodas, E. M., Lohan, M., Geibere, W., Tagliabu
- e, A., Bowie, A., Jeandel, C., Maldonado, M. T., Landing, W. M., Cockw
- ell, D., Abadie, C., Abouchami, W., Achterberg, E. P., Agather, A., Agulia
- 1074 r-Islas, A., van Aken, H. M., Andersen, M., Archer, C., Auro, M., de Baa
- 1075 r, H. J., Baars, O., Baker, A. R., Bakker, K., Basak, C., Baskaran, M., Ba
- tes, N. R., Bauch, D., van Beek, P., Behrens, M. K., Black, E., Bluhm,
- 1077 K., Bopp, L., Bouman, H., Bowman, K., Bown, J., Boyd, P., Boye, M., B
- oyle, E. A., Branellec, P., Bridgestock, L., Brissebrat, G., Browning, T., B
- ruland, K. W., Brumsack, H.-J., Brzezinski, M., Buck, C. S., Buck, K. N.,
- Buesseler, K., Bull, A., Butler, E., Cai, P., Camara Mor, P., Cardinal, D.,
- Carlson, C., Carrasco, G., Casacuberta, N., Casciotti, K. L., Castrillejo, M.,
- 1082 Chamizo, E., Chance, R., Charette, M. A., Chaves, J. E., Cheng, H., Che
- ver, F., Christl, M., Church, T. M., Closset, I., Colman, A., Conway, T.
- M., Cossa, D., Croot, P., Cullen, J. T., Cutter, G. A., Daniels, C., Dehairs,

F., Deng, F., Dieu, H. T., Duggan, B., Dulaquais, G., Dumousseaud, C., 1085 Echegoyen-Sanz, Y., Edwards, R. L., Ellwood, M., Fahrbach, E., Fitzsimm 1086 ons, J. N., Flegal, A. R., Fleisher, M. Q., van de Flierdt, T., Frank, M., F 1087 riedrich, J., Fripiat, F., Froellje, H., Galer, S. J. G., Gamo, T., Ganeshram, 1088 R. S., Garcia-Orellana, J., Garcia-Solsona, E., Gault-Ringold, M., George, 1089 E., Gerringa, L. J. A., Gilbert, M., Godoy, J. M., Goldstein, S. L., Gonzal 1090 ez, S. R., Grissom, K., Hammerschmidt, C., Hartman, A., Hassler, C. S., 1091 Hathorne, E. C., Hatta, M., Hawco, N., Hayes, C. T., Heimburger, L.-E., 1092 Helgoe, J., Heller, M., Henderson, G. M., Henderson, P. B., van Heuven, 1093 S., Ho, P., Horner, T. J., Hsieh, Y.-T., Huang, K.-F., Humphreys, M. P., Is 1094 shiki, K., Jacquot, J. E., Janssen, D. J., Jenkins, W. J., John, S., Jones, E. 1095 M., Jones, J. L., Kadko, D. C., Kayser, R., Kenna, T. C., Khondoker, R., 1096 Kim, T., Kipp, L., Klar, J. K., Klunder, M., Kretschmer, S., Kumamoto, 1097 Y., Laan, P., Labatut, M., Lacan, F., Lam, P. J., Lambelet, M., Lamborg, 1098 C. H., Le Moigne, F. A. C., Le Roy, E., Lechtenfeld, O. J., Lee, J.-M., L 1099 herminier, P., Little, S., Lopez-Lora, M., Lu, Y., Masque, P., Mawji, E., M 1100 cClain, C. R., Measures, C., Mehic, S., Menzel Barraqueta, J.-L., van der 1101 Merwe, P., Middag, R., Mieruch, S., Milne, A., Minami, T., Moffett, J. 1102 W., Moncoiffe, G., Moore, W. S., Morris, P. J., Morton, P. L., Nakaguchi, 1103 Y., Nakayama, N., Niedermiller, J., Nishioka, J., Nishiuchi, A., Noble, A., 1104 Obata, H., Ober, S., Ohnemus, D. C., van Ooijen, J., O'Sullivan, J., Owe 1105 ns, S., Pahnke, K., Paul, M., Pavia, F., Pena, L. D., Petersh, B., Planchon, 1106

- F., Planquette, H., Pradoux, C., Puigcorbe, V., Quay, P., Queroue, F., Rad 1107 ic, A., Rauschenberg, S., Rehkamper, M., Rember, R., Remenyi, T., Resin 1108 g, J. A., Rickli, J., Rigaud, S., Rijkenberg, M. J. A., Rintoul, S., Robinso 1109 n, L. F., Roca-Marti, M., Rodellas, V., Roeske, T., Rolison, J. M., Rosenb 1110 erg, M., Roshan, S., van der Loaff, M. M. R., Ryabenko, E., Saito, M. 1111 A., Salt, L. A., Sanial, V., Sarthou, G., Schallenberg, C., Schauer, U., Sch 1112 er, H., Schlosser, C., Schnetger, B., Scott, P., Sedwick, P. N., Semiletov, I., 1113 Shelley, R., Sherrell, R. M., Shiller, A. M., Sigman, D. M., Singh, S. K., 1114 Slagter, H. A., Slater, E., Smethie, W. M., Snaith, H., Sohrin, Y., Sohst, 1115 B., Sonke, J. E., Speich, S., Steinfeldt, R., Stewart, G., Stichel, T., Stirlin 1116 g, C. H., Stutsman, J., Swarr, G. J., Swift, J. H., Thomas, A., Thorne, K., 1117 Till, C. P., Till, R., Townsend, A. T., Townsend, E., Tuerena, R., Twinin 1118 g, B. S., Vance, D., Velazquez, S., Venchiarutti, C., Villa-Alfageme, M., V 1119 ivancos, S. M., Voelker, A. H. L., Wake, B., Warner, M. J., Watson, R., v 1120 an Weerlee, E., Weigand, M. A., Weinstein, Y., Weiss, D., Wisotzki, A., 1121 Woodward, E. M. S., Wu, J., Wu, Y., Wuttig, K., Wyatt, N., Xiang, Y., X 1122 ie, R. C., Xue, Z., Yoshikawa, H., Zhang, J., Zhang, P., Zhao, Y., Zheng, 1123
- Zurbrick, C.: The GEOTRACES Intermediate Data Product 2017, CHEMIC AL GEOLOGY, 493, 210-223, 10.1016/j.chemgeo.2018.05.040, 2018.

L., Zheng, X.-Y., Zieringer, M., Zimmer, L. A., Ziveri, P., Zunino, P., and

Shaked, Y., Kustka, A. B., and Morel, F. M. M.: A general kinetic model for iron acquisition by eukaryotic phytoplankton, Limnol. Oceanogr., 50, 872-8

- 1129 82, 10.4319/lo.2005.50.3.0872, 2005.
- 1130 Shi, Z., Krom, M. D., Bonneville, S., Baker, A. R., Jickells, T. D., and Benni
- 1131 ng, L. G.: Formation of Iron Nanoparticles and Increase in Iron Reactivity
- in Mineral Dust during Simulated Cloud Processing, Environ. Sci. Techno
- 1133 1, 43, 6592-6596, 10.1021/es901294g, 2009.
- 1134 Shi, Z., Krom, M. D., Jickells, T. D., Bonneville, S., Carslaw, K. S., Mihalopo
- ulos, N., Baker, A. R., and Benning, L. G.: Impacts on iron solubility in
- the mineral dust by processes in the source region and the atmosphere: A
- review, Aeolian Res., 5, 21-42, 10.1016/j.aeolia.2012.03.001, 2012.
- 1138 Shi, Z. B., Woodhouse, M. T., Carslaw, K. S., Krom, M. D., Mann, G. W., B
- aker, A. R., Savov, I., Fones, G. R., Brooks, B., Drake, N., Jickells, T.
- D., and Benning, L. G.: Minor effect of physical size sorting on iron solu
- bility of transported mineral dust, Atmos. Chem. Phys., 11, 8459-8469, 10.
- 1142 5194/acp-11-8459-2011, 2011a.
- Shi, Z., Krom, M. D., Bonneville, S., Baker, A. R., Bristow, C., Drake, N., M
- ann, G., Carslaw, K., McQuaid, J. B., Jickells, T., and Benning, L. G.: Inf
- luence of chemical weathering and aging of iron oxides on the potential ir
- on solubility of Saharan dust during simulated atmospheric processing, Glo
- bal Biogeochem. Cycles, 25, 10.1029/2010GB003837, 2011b.
- Shoenfelt, E. M., Winckler, G., Annett, A. L., Hendry, K. R., and Bostick, B.
- 1149 C.: Physical Weathering Intensity Controls Bioavailable Primary Iron (II) S
- ilicate Content in Major Global Dust Sources, Geophys. Res. Lett., 46, 10

- 1151 854-10864, 10.1029/2019GL084180, 2019.
- Siegel, D. A., Buesseler, K. O., Doney, S. C., Sailley, S. F., Behrenfeld, M. J.,
- and Boyd, P. W.: Global assessment of ocean carbon export by combinin
- g satellite observations and food-web models, Global Biogeochem. Cycles,
- 28, 181-196, 10.1002/2013GB004743, 2014.
- Spolaor, A., Vallelonga, P., Cozzi, G., Gabrieli, J., Varin, C., Kehrwald, N., Ze
- nnaro, P., Boutron, C., and Barbante, C.: Iron speciation in aerosol dust in
- fluences iron bioavailability over glacial-interglacial timescales, Geophys. R
- es. Lett., 40, 1618-1623, 10.1002/grl.50296, 2013.
- Struve, T., Longman, J., Zander, M., Lamy, F., Winckler, G., and Pahnke, K.:
- Systematic changes in circumpolar dust transport to the Subantarctic Pacifi
- 1162 c Ocean over the last two glacial cycles, Proc. Natl. Acad. Sci. U.S.A., 1
- 1163 19, 10.1073/pnas.2206085119, 2022.
- 1164 Sunda W. G. & Huntsman, S. A.: Iron uptake and growth limitation in oceani
- c and coastal phytoplankton, Mar Chem, 50, 189-206, 10.1016/0304-4203(9
- 1166 5)00035-P, 1995.
- 1167 Tagliabue, A., Bowie, A. R., Boyd, P. W., Buck, K. N., Johnson, K. S., and S
- aito, M. A.: The integral role of iron in ocean biogeochemistry, Nature, 5
- 43, 51-59, 10.1038/nature21058, 2017.
- 1170 Tagliabue, A., Aumont, O., DeAth, R., Dunne, J. P., Dutkiewicz, S., Galbraith,
- E., Misumi, K., Moore, J. K., Ridgwell, A., Sherman, E., Stock, C., Vichi,
- M., Voelker, C., and Yool, A.: How well do global ocean biogeochemistr

- y models simulate dissolved iron distributions? Global Biogeochem. Cycles,
- 1174 30, 149-174, 10.1002/2015GB005289, 2016.
- 1175 Tegen, I., Werner, M., Harrison, S. P., and Kohfeld, K. E.: Relative importance
- of climate and land use in determining present and future global soil dus
- t emission, Geophys. Res. Lett., 31, 10.1029/2003GL019216, 2004.
- 1178 Trapp, J. M., Millero, F. J., and Prospero, J. M.: Trends in the solubility of ir
- on in dust-dominated aerosols in the equatorial Atlantic trade winds: Impo
- 1180 rtance of iron speciation and sources, Geochem. Geophys. Geosystems, 11,
- 1181 10.1029/2009GC002651, 2010.
- Twining, B. S., Rauschenberg, S., Morton, P. L., and Vogt, S.: Metal contents
- of phytoplankton and labile particulate material in the North Atlantic Ocea
- n, Prog. Oceanogr., 137, 261-283, 10.1016/j.pocean.2015.07.001, 2015.
- Wang, N. and Zhang, Y.: Long-term variations of global dust emissions and cli
- mate control, Environ. Pollut., 340, 10.1016/j.envpol.2023.122847, 2024.
- Watson, A. J., Bakker, D. C. E., Ridgwell, A. J., Boyd, P. W., and Law, C. S.:
- Effect of iron supply on Southern Ocean CO₂ uptake and implications fo
- r glacial atmospheric CO₂, Nature, 407, 730-733, 10.1038/35037561, 2000.
- Westberry, T. K., Behrenfeld, M. J., Shi, Y. R., Yu, H., Remer, L. A., and Bia
- 1191 n, H.: Atmospheric nourishment of global ocean ecosystems, Science, 380,
- 1192 515-519, 10.1126/science.abq5252, 2023.
- 1193 Wiseman, N. A., Moore, J. K., Twining, B. S., Hamilton, D. S., and Mahowal
- d, N. M.: Acclimation of phytoplankton Fe:C ratios dampens the biogeoch

- emical response to varying atmospheric deposition of soluble iron, Global
- Biogeochem. Cycles, 37, 10.1029/2022GB007491, 2023.
- Wolff, E. W., Barbante, C., Becagli, S., Bigler, M., Boutron, C. F., Castellano,
- E., de Angelis, M., Federer, U., Fischer, H., Fundel, F., Hansson, M., Hutt
- erli, M., Jonsell, U., Karlin, T., Kaufmann, P., Lambert, F., Littot, G. C.,
- Mulvaney, R., Roethlisberger, R., Ruth, U., Severi, M., Siggaard-Andersen,
- 1201 M. L., Sime, L. C., Steffensen, J. P., Stocker, T. F., Traversi, R., Twarloh,
- B., Udisti, R., Wagenbach, D., and Wegner, A.: Changes in environment
- over the last 800,000 years from chemical analysis of the EPICA Dome C
- ice core, Quat. Sci. Rev., 29, 285-295, 10.1016/j.quascirev.2009.06.013, 20
- 1205 10.
- 1206 Zender, C. S., Bian, H. S., and Newman, D.: Mineral Dust Entrainment and D
- eposition (DEAD) model: Description and 1990s dust climatology, J. Geop
- 1208 hys. Res. Atmos., 108, 10.1029/2002JD002775, 2003.
- 1209 Zhang, C., Yao, X., Chen, Y., Chu, Q., Yu, Y., Shi, J., and Gao, H.: Variation
- s in the phytoplankton community due to dust additions in eutrophication,
- LNLC and HNLC oceanic zones, Sci. Total Environ., 669, 282-293, 10.10
- 1212 16/j.scitotenv.2019.02.068, 2019.
- 1213 Zhang, Y., Mahowald, N., Scanza, R. A., Journet, E., Desboeufs, K., Albani,
- 1214 S., Kok, J. F., Zhuang, G., Chen, Y., Cohen, D. D., Paytan, A., Patey, M.
- D., Achterberg, E. P., Engelbrecht, J. P., and Fomba, K. W.: Modeling th
- e global emission, transport and deposition of trace elements associated wi

1217	th mineral dust, Biogeosciences, 12, 5771-5792, 10.5194/bg-12-5771-2015,
1218	2015.
1219	Zheng, Y., Zhao, T., Che, H., Liu, Y., Han, Y., Liu, C., Xiong, J., Liu, J., and
1220	Zhou, Y.: A 20-year simulated climatology of global dust aerosol depositi
1221	on, Sci. Total Environ., 557, 861-868, 10.1016/j.scitotenv.2016.03.086, 2016
1222	Ziegler, M., Diz, P., Hall, I. R., and Zahn, R.: Millennial-scale changes in atm
1223	ospheric CO2 levels linked to the Southern Ocean carbon isotope gradient
1224	and dust flux, Nat. Geosci., 6, 457-461, 10.1038/NGEO1782, 2013.
1225	
1226	
1227	

Tables
 Table 1 List of abbreviations and full terms for dust source regions and oceans

Dust source regions/ oceans	Full terms	Abbreviations
Dust source regions	Northwest Africa	NWAf
	Northeast Africa	NEAf
	Middle Africa	MAf
	South Africa	SAf
	North America	NAm
	South America	SAm
	West Asia	WAs
	Middle-North Asia	MNAs
	East Asia	EAs
	South Asia	SAs
	Australia	AU
Oceans	North Pacific Ocean	NP
	North Atlantic Ocean	NA
	Mediterranean Sea	MS
	Southern Ocean	SO
	Equatorial Pacific Ocean	EP
	Equatorial Atlantic Ocean	EA
	Equatorial Indian Ocean	EI
	Red Sea	RS
	high nutrient, low chlorophyll regions in Equatorial Pacific Ocean	HNLC_EP
	high nutrient, low chlorophyll regions in North Pacific Ocean	HNLC_NP

1230 Figures

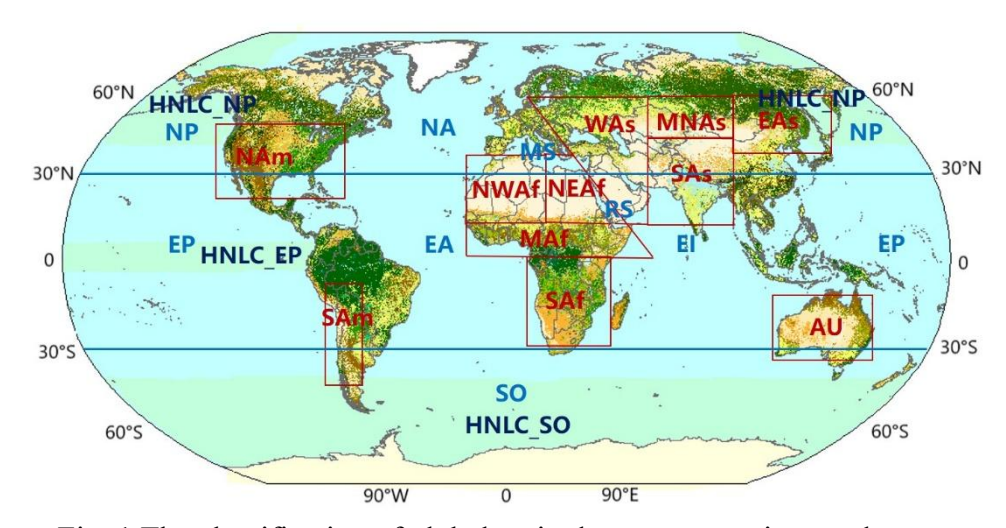


Fig. 1 The classification of global main dust source regions and oceans (Dust source regions: NWAf - Northwest Africa; NEAf - Northeast Africa; MAf - Middle Africa; SAf - South Africa; NAm - North America; SAm - South America; WAs - West Asia; MNAs - Middle-North Asia; EAs - East Asia; SAs - South Asia; AU - Australia.)

(Oceans: NP - North Pacific Ocean; NA - North Atlantic Ocean; MS - Mediterranean Sea; RS - Red Sea; SO - Southern Ocean; EP - Equatorial Pacific Ocean; EA - Equatorial Atlantic Ocean; EI - Equatorial Indian Ocean; HNLC_EP - high nutrient, low chlorophyll regions in Equatorial Pacific Ocean; HNLC_NP - high nutrient, low chlorophyll regions in North Pacific Ocean.)

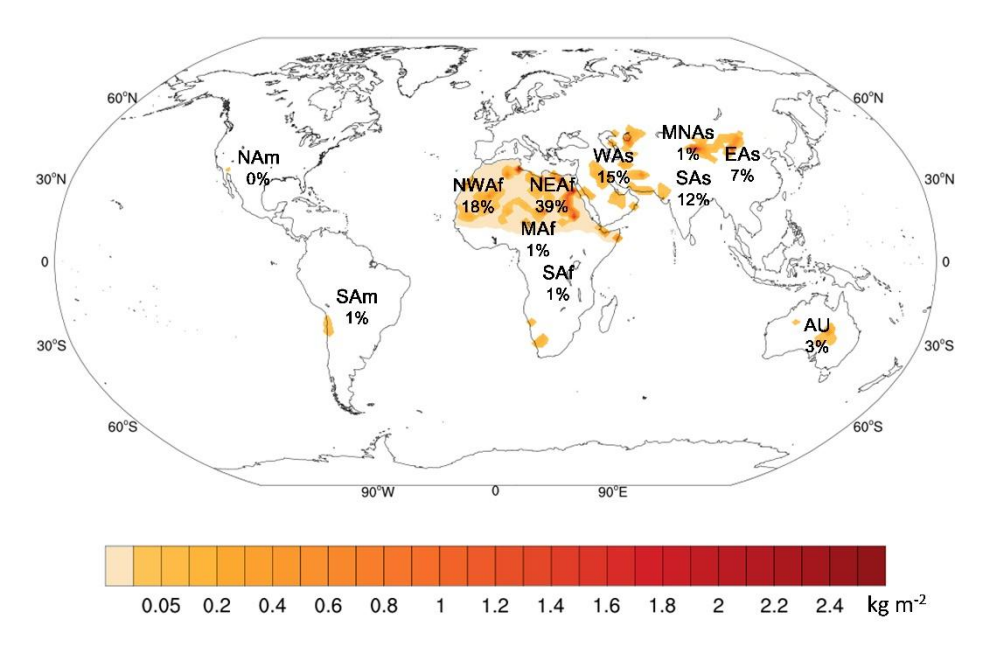


Fig. 2 The spatial distribution and proportion of the global five-year average dust emission, and percentages show the proportions of annual dust emission of each dust source to global (Dust source regions: NWAf - Northwest Africa; NEAf - Northeast Africa; MAf - Middle Africa; SAf - South Africa; NAm - North America; SAm - South America; WAs - West Asia; MNAs - Middle-North Asia; EAs - East Asia; SAs - South Asia; AU - Australia.)

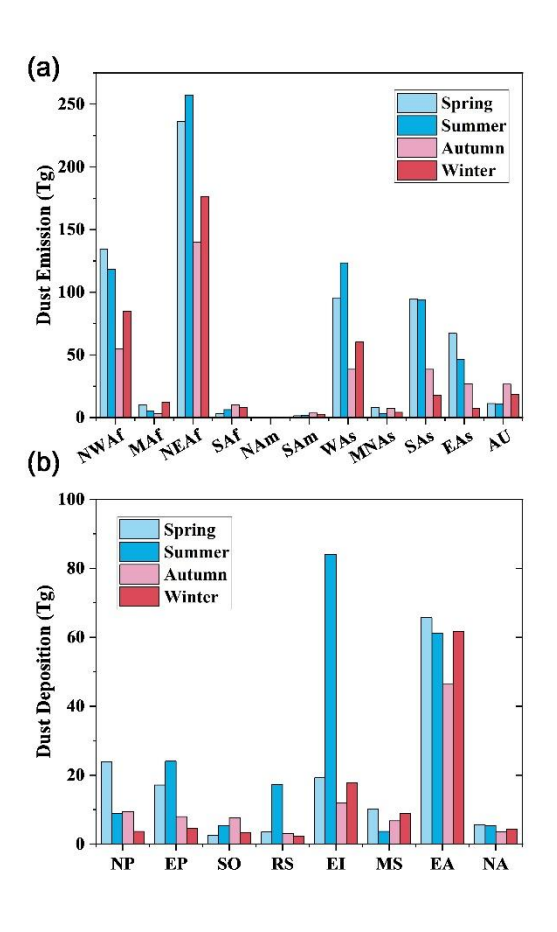


Fig. 3 The seasonal variations of (a) dust emission and (b) deposition i n various dust sources

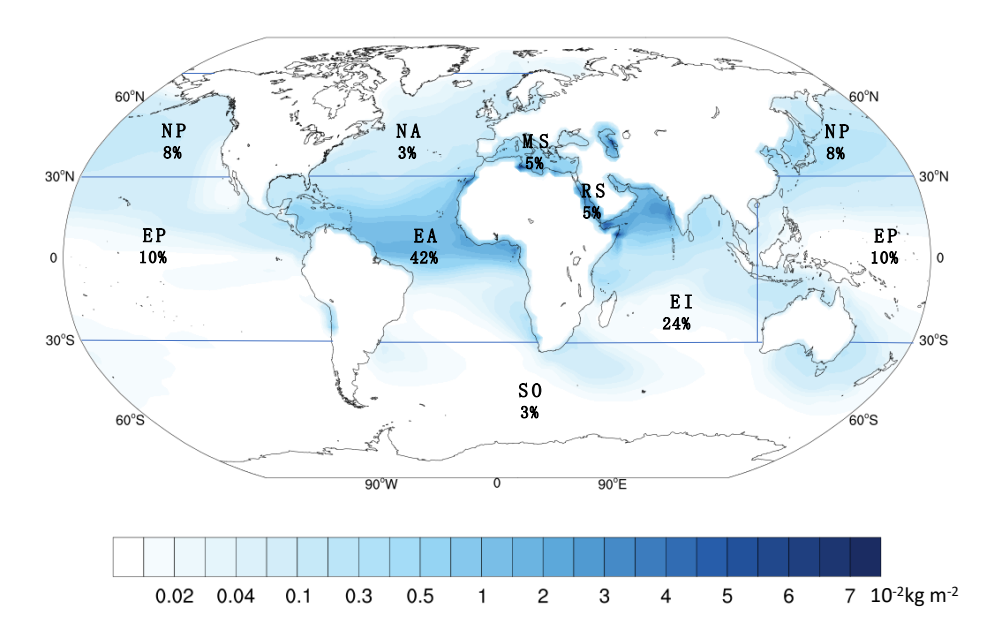


Fig. 4 The spatial distribution and proportion of the global five-year average dust deposition. Blue lines together with land-sea boundaries indicate different ocean regions. The percentages express the proportions of annual dust deposition in each ocean to global ocean (Oceans: NP - North Pacific Ocean; NA - North Atlantic Ocean; MS - Mediterranean Sea; RS - Red Sea; SO - Southern Ocean; EP - Equatorial Pacific Ocean; EA - Equatorial Atlantic Ocean; EI - Equatorial Indian Ocean.)

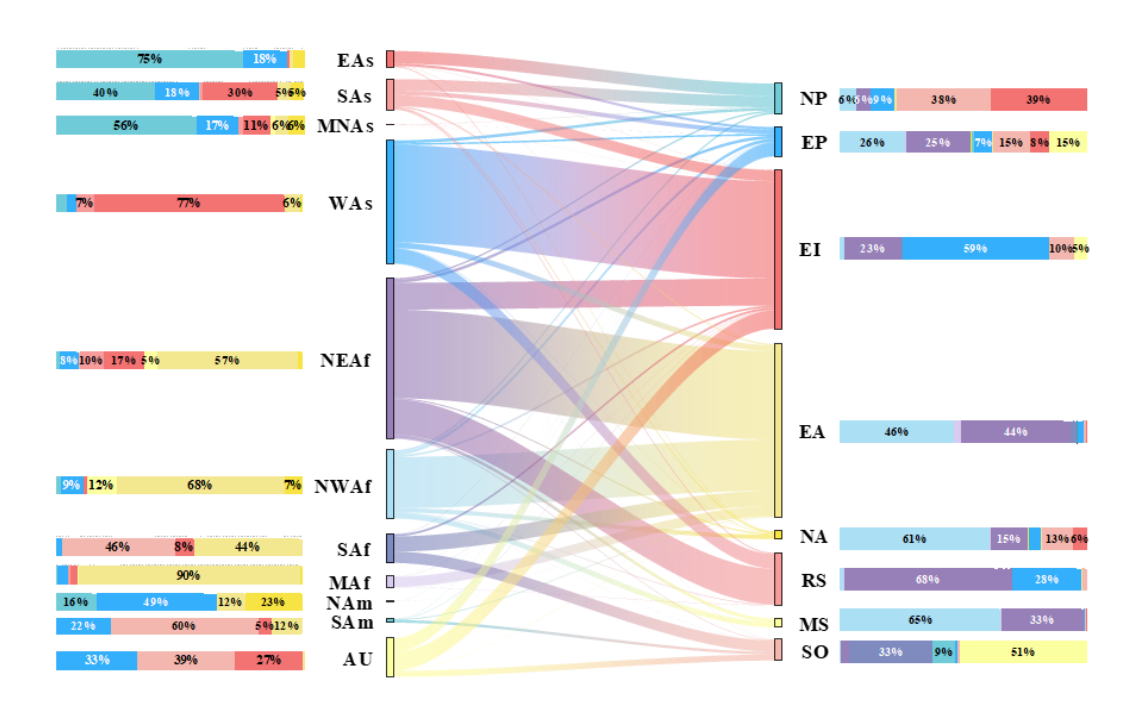


Fig. 5 The annual contributions of various dust source regions to oceanic dust deposition

Each column on the left represents the fraction of dust emitted from a given source region that is ultimately deposited in individual oceans, with different colors indicating the respective oceans. Each column on the right shows the contributions of various dust source regions to dust deposition over each ocean, with different colors corresponding to different dust source regions. The longitudinal columns depict the proportions of dust emission or deposition relative to global marine dust deposition. The lines in the middle illustrate the transport direction and intensity.

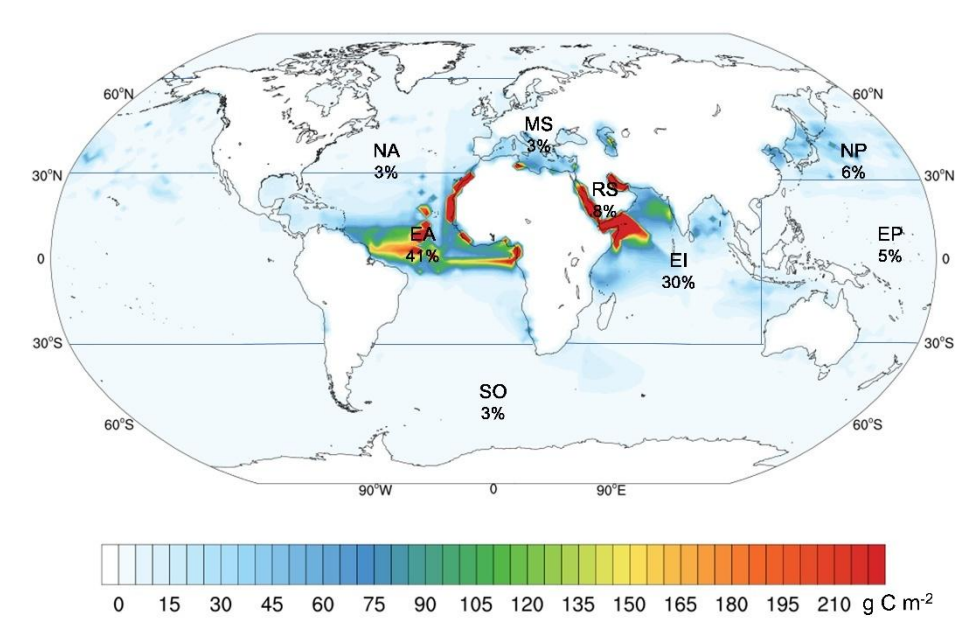


Fig. 6 The annual phytoplankton carbon uptake induced by dust deposition. Blue lines together with land-sea boundaries indicate different ocean regions. The percentages represent the proportion of annual dust-driven phytoplankton carbon uptake in each ocean to global ocean

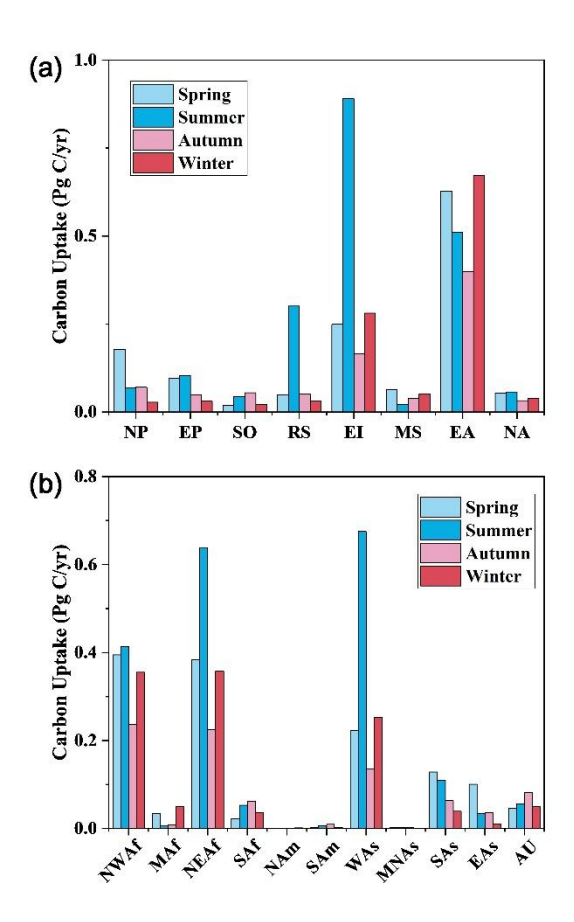


Fig. 7 (a) Seasonal variations of marine phytoplankton carbon uptake caused by dust deposition over each ocean area;

(b) Seasonal contribution of dust source regions to marine phytoplankton carbon uptake driven by dust deposition

1247

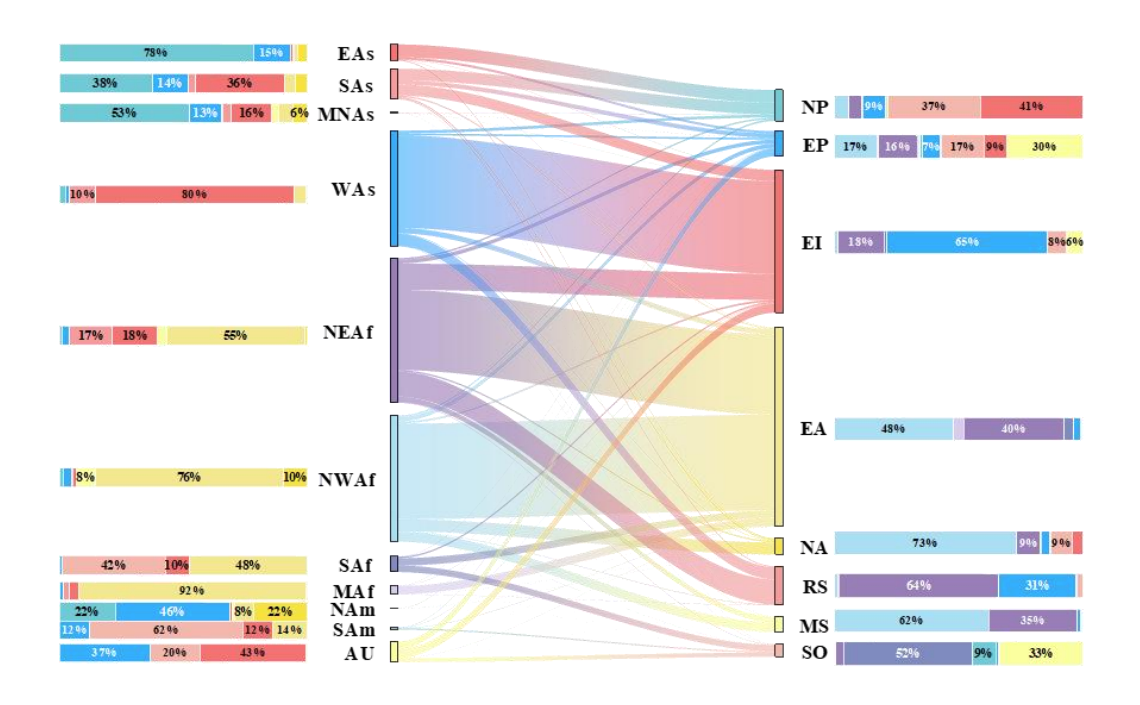


Fig. 8 The annual contribution of various dust source regions to the marine carbon uptake

Each column on the left represents the fraction of dust emitted from a given source region that ultimately induces phytoplankton carbon uptake in individual oceans, with different colors indicating the corresponding oceans. Each column on the right shows the contributions of various dust source regions to phytoplankton carbon uptake driven by dust deposition over each ocean, with different colors representing the respective dust sources. The longitudinal columns display the contribution ratios of dust sources or oceans to the total marine phytoplankton carbon uptake driven by dust deposition. The lines in the middle illustrate the transport direction and intensity.